Computer Methods in Applied Mechanics and Engineering 456 (2026) 118942

Contents lists available at ScienceDirect

Comput. Methods Appl. Mech. Engrg.

journal homepage: www.elsevier.com/locate/cma

Origins of phase-field crack widening in dynamic fragmentation explained

Shad Durussel [a,*], Gergely Molnár [b], Jean-François Molinari [a]

[a] Institute of Civil Engineering, Institute of Materials Science and Engineering, Ecole Polytechnique Fédérale de Lausanne (EPFL),1015, Lausanne, Switzerland
[b] CNRS, INSA Lyon, LaMCoS, UMR5259, 69621 Villeurbanne, France

ARTICLE INFO

Keywords:
Phase-field fracture
Dynamic fragmentation
Mass erosion
Branching
Wave-damage interaction

ABSTRACT

We investigate dynamic crack propagation and fragmentation with the phase-field fracture approach. The method was chosen for its ability to yield crack paths that are independent of the underlying mesh, thanks to the damage regularization zone. In dynamics, we observe a progressive widening of this regularization zone and attribute it to an unphysical trapping of elastic waves. We show that the damage zones do not represent free boundaries accurately and that wave interactions induce additional damage. We reveal how mass erosion, by conserving the elastic wave speed in the damaged regions, can be used to efficiently reduce the spurious diffusion of damage. Furthermore, we provide numerical evidence that dynamically propagating cracks in the phase-field formulation, both with and without mass erosion, converge to the predictions of linear elastic fracture mechanics. For vanishing regularization length, the crack speed and energy release rate become independent of the phase-field regularization length, provided that this length scale is small enough and the mesh fine enough to resolve the process zone.

1. Introduction

Dynamic fragmentation refers to the rapid breakup of a solid into multiple fragments resulting from the sudden release of a large amount of energy, such as during an impact or an explosion. The study of this phenomenon has a wide range of applications, from improving the safety of tempered glass [1–3] to mitigating the risks associated with space debris [4,5].

Theoretical fragmentation models were developed to predict fragment size distributions under dynamic loading, initially using a statistical approach [6] and later extended to energy-driven models [7–9]. The complexity and variability of real-world scenarios, however, motivate the use of computational models that can accommodate more complex geometries, loading conditions, and material behaviour. The end goal is to accurately capture the elastodynamics as well as the fracture mechanics leading to crack nucleation and propagation (including branching), which collectively shape the final fragments size distribution.

Discrete element simulations have demonstrated that even relatively simple particle models can reproduce key statistical features of fragmentation, such as power-law fragment size distributions following impacts or internal explosions in solid bodies [10,11]. In contrast, mesh-based numerical fracture models are able to describe the formation and evolution of individual cracks that ultimately lead to fragmentation. These fracture models can be broadly classified into two main categories.

The first category comprises methods based on a discrete representation of discontinuities. For instance, the extended finite element method (XFEM) enriches the interpolation space to allow for the discrete representation of cracks without remeshing [12],

* corresponding author.
E-mail addresses: shad.durussel@epfl.ch (S. Durussel), gergely.molnar@insa-lyon.fr (G. Molnár), jean-francois.molinari@epfl.ch (J.-F. Molinari).

https://doi.org/10.1016/j.cma.2026.118942
Received 19 December 2025; Received in revised form 4 March 2026; Accepted 21 March 2026
Available online 29 March 2026

but requires additional criteria to handle crack branching [13]. Cohesive zone models (CZM) provide an explicit representation of cracks and fragments through topological changes in the mesh [14,15], either along predefined crack paths [16] or via the automatic insertion of cohesive elements [17]. This makes CZM particularly well suited for the study of fragmentation [2,18–20]. However, without remeshing, this method remains mesh dependent, which limits the robustness of fracture path predictions and, consequently, of the resulting fragment shapes.

The second category includes models based on a smeared representation of cracks. Representative examples include nonlocal integral approaches [21,22], peridynamics [23], thick level-set methods [24], and the Lip-field approach [25] amongst others. Phase-field modelling of fracture also falls within this category. As with other smeared approaches, phase-field methods are attractive for their independence from the underlying mesh topology, but they require sufficiently fine mesh resolution to accurately capture the transition from intact to fully broken material. Phase-field fracture models were developed within both the physics community, through Ginzburg-Landau-type phase-transition formulations [26,27], and the mechanics community, through variational formulations of brittle fracture based on Griffith's theory [28,29] and their regularized approximations [30,31]. The crack thickness in phase-field models can be interpreted in two ways: as a purely numerical regularization that should vanish as the regularization length is refined, or as a genuine material parameter [32]. This approach has since been adapted to a wide range of fracture applications, including ductile fracture [33] and stochastic modelling of brittle fracture [34].

The extension of the phase-field framework to dynamic crack propagation [35,36] has opened the door to its application to dynamic fragmentation, and it has already been used to study one-dimensional fragmentation [37,38]. However, a widening of damage bands is commonly observed under dynamic loading [35,36]. As this widening appears to be load-dependent, it becomes particularly problematic in the context of dynamic fragmentation, where extreme loading can lead to uninterpretable and potentially unphysical damage patterns. Moreover, because the damaged material is progressively degraded, elastic waves are reflected by a diffusive interface, potentially leading to additional damage and spalling through wave superposition [39]. This suggests that the interaction between elastic waves and damaged zones is a key mechanism in the development of this damage sprawl.

As material stiffness is degraded, the wave speed within the damaged zone decreases, and elastic waves interact with damage. The objective of this work is to compare the classical phase-field formulation with an alternative approach that preserves the wave velocity by degrading the mass consistently with the stiffness. After illustrating the issue in a fragmentation example, we investigate the interaction between an elastic wave and a damaged boundary in a pseudo one-dimensional setting and explore, how damage spreads through this interaction.

The differences in crack propagation dynamics between the two approaches are then examined in two dimensions, first for a single crack and then in the presence of branching. In this context, we study the convergence of the crack velocity and the dissipated energy as the regularization length is reduced.

This article begins by recalling the formulation of phase-field modelling of fracture in Section 2. In Section 3, we illustrate the issue of damage-band widening in fragmentation. The interaction between elastic waves and damage, as well as the resulting damage sprawl, is then explored in Section 4. In Section 5, we investigate the behaviour of the model with mass degradation in the context of two-dimensional crack propagation and branching. Finally, Section 6 discusses the perspectives opened by these results and outlines potential directions for future research.

2. Phase-field modelling of brittle fracture

2.1. Regularized variational formulation of Griffith energy balance

Starting from the free-discontinuity framework, brittle fracture can be described by the variational formulation introduced by Francfort and Marigo [29]. In this setting, the displacement field $\mathbf{u}$ and the crack set Γ are obtained by minimizing the total energy functional

$$E(\mathbf{u},\Gamma) = \int_{\Omega\setminus\Gamma} \Psi(\boldsymbol{\varepsilon}(\mathbf{u}))\, dV + G_c \mathcal{H}^{n-1}(\Gamma), \tag{1}$$

where Ω denotes the domain of interest and Γ represents a set of discontinuities corresponding to cracks. The first term accounts for the elastic strain energy stored in the intact region $\Omega \setminus \Gamma$, with $\Psi(\varepsilon)$ the strain-energy density expressed in terms of the linearized strain tensor $\varepsilon(\mathbf{u})$. The second term represents the fracture energy required to create new crack surfaces. It is proportional to the critical energy release rate G_c, and to $\mathcal{H}^{n-1}(\Gamma)$, the $(n-1)$-dimensional Hausdorff measure quantifying the total crack surface.

Regularization of the free-discontinuity problem follows the framework introduced in Ref. [30]. In particular, the work of Bourdin et al. [31] proposes a variational regularization based on a scalar damage field $d(\mathbf{x}) \in [0,1]$, where $d = 0$ denotes undamaged material, $d = 1$ corresponds to fully damaged material, and intermediate values describe a diffusive transition zone. This transition from a sharp discontinuity to a smeared description of the crack is illustrated in Fig. 1a. The regularized energy functional is given by

$$E_{l_0}(\mathbf{u},d) = \int_\Omega g(d)\Psi(\boldsymbol{\varepsilon}(\mathbf{u}))\, dV + \frac{G_c}{c_w}\int_\Omega \left(\frac{w(d)}{l_0} + l_0|\nabla d|^2\right) dV, \tag{2}$$

where the Hausdorff measure in Eq. (1) is approximated by a volumetric integral. Note that there exists a higher order formulation for the said volumetric integral, such as the fourth-order formulation incorporating a term in $|\Delta d|^2$ [40]. The length scale parameter l_0 governs the thickness of the diffusive crack region, i.e. the width of the transition zone between $d = 0$ and $d = 1$. The degradation function $g(d)$ is a continuous, monotonically decreasing function that reduces the material stiffness as damage grows, and satisfies

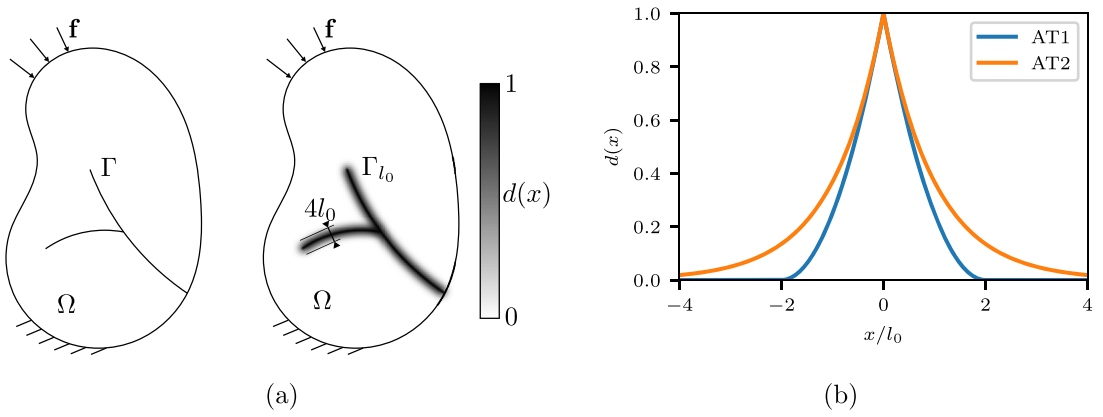

Fig. 1. (a)Regularization of a sharp crack Γ by a diffusive damage field $d(\mathbf{x})$ in a continuous domain Ω subject to traction $\mathbf{f}$ and imposed displacement. The regularized fracture corresponds to the region $\Gamma_{l_0} = \{\mathbf{x} \in \Omega | d(\mathbf{x}) > 0\}$ of width related to l_0. (b)Optimal damage profile for a 1D crack located at $x = 0$. Note the limited support of the damage for the AT1 formulation.

$g(0) = 1 g(1) = 0, g'(1) = 0$ and $g'(d) < 0$ for $d \in [0, 1)$. A widely used choice for this function is the quadratic polynomial

$$g(d) = (1 - d)^2. \tag{3}$$

The local contribution to the dissipated energy is described by a continuous and monotonic function $w(d)$ satisfying $w(0) = 0, w(1) = 1$ and $w'(d) \geq 0$ for $d \in [0, 1]$. This function is associated with a normalization constant defined as $c_w := 4 \int_0^1 \sqrt{w(s)} ds$.

The original formulation in [31] gives $w(d) = d^2$ and $c_w = 2$. In [41], a linear function is proposed for the dissipated energy. These two formulations are commonly referred to as AT2 and AT1, respectively:

- AT1: $w(d) = d, \quad c_w = \frac{8}{3}$
- AT2: $w(d) = d^2, \quad c_w = 2$

The optimal damage profile for a one-dimensional crack located at $x = 0$ is shown in Fig. 1b for both the AT1 and AT2 formulations.

The main difference between the two models is that AT1 presents a limited support for the damage around a crack and predicts an initial purely elastic phase prior to damage nucleation, whereas AT2 produces a gradual degradation of stiffness from the onset of loading. The inherent positivity of the damage variable in AT2, resulting from the squared term in the dissipation function, is often considered an attractive feature. However, in dynamic applications it is desirable to preserve the undamaged elastic response and the correct wave speed away from the crack, which makes the AT1 formulation more suitable in that context. Hence, this is the formulation that will be used for the entirety of this study.

The problem is extended to dynamic by accounting the contribution of the kinetic energy to the total energy functional. Subtracting also the work from external forces $W_{\text{ext}}(\mathbf{u})$ gives

$$E_{l_0}(\mathbf{u}, d) = \int_\Omega g(d) \Psi(\boldsymbol{\varepsilon}(\mathbf{u})) \, dV + \frac{G_c}{c_w} \int_\Omega \left(\frac{w(d)}{l_0} + l_0 \|\nabla d\|^2 \right) dV - \int_\Omega \frac{1}{2} \rho \ddot{\mathbf{u}} \cdot \dot{\mathbf{u}} \, dV - W_{\text{ext}}(\mathbf{u}), \tag{4}$$

with ρ the mass density of the material.

For an arbitrary time interval, we can now define the space-time action integral

$$A(\mathbf{u}, d) = \int_{t_0}^{t_1} E_{l_0}(\mathbf{u}, d) \, dt. \tag{5}$$

The coupled displacement-damage problem is subject to the three following principles:

- Irreversibility of damage: $\dot{d} \geq 0$ for all time t
- First-order stability: the action-integral variation is non-negative with respect to arbitrary variations of admissible displacements and damage evolution,

$$A'(\mathbf{u}, d)(\hat{\mathbf{u}} - \mathbf{u}, \hat{d} - d) \geq 0, \quad \forall \hat{\mathbf{u}} \in \mathcal{U}(\mathbf{u}), \hat{d} \in D(d). \tag{6}$$

  The spaces $\mathcal{U}(\mathbf{u}) = \left\{ \hat{\mathbf{u}} : \Omega \times [t_0, t_1] \to \mathbb{R}^{\dim} | \hat{\mathbf{u}} = \mathbf{u}_0 \text{ on } \partial\Omega_u \right\}$ and $D(d) = \left\{ \hat{d} : \Omega \times [t_0, t_1] \to [0, 1] | 0 \leq d \leq \hat{d} \leq 1 \right\}$ are the admissible spaces of displacements and damage, respectively, $\mathbf{u}_0$ being a prescribed displacement on a subset $\partial\Omega_u$ of the geometric space.
- Energy balance: damage is the only source of energy dissipation via the fracture energy $E_{\text{frac}}(\mathbf{u}, d) = \frac{G_c}{c_w} \int_\Omega \left(\frac{w(d)}{l_0} + l_0 \|\nabla d\|^2 \right) dV$.

The derivation of the second principle at fixed damage leads to the damage-dependent elastodynamic equilibrium

$$\nabla \cdot \boldsymbol{\sigma}(\mathbf{u}, d) + \mathbf{b} = \rho \ddot{\mathbf{u}}, \tag{7}$$

with appropriate boundary condition $\boldsymbol{\sigma}\mathbf{n} = \mathbf{f}$ on $\partial\Omega_f$, $\mathbf{n}$ being the outward normal vector, and the body forces $\mathbf{b}$. The stress function is derived from the elastic energy

$$\boldsymbol{\sigma}(\mathbf{u}, d) = (1-d)^2 \frac{\partial \Psi(\boldsymbol{\varepsilon}(\mathbf{u}))}{\partial \boldsymbol{\varepsilon}} = (1-d)^2(\lambda \mathrm{tr}(\boldsymbol{\varepsilon})\mathbf{I} + 2\mu\boldsymbol{\varepsilon}), \tag{8}$$

λ and μ being the Lamé parameters.

The time dependence of damage being only induced by its irreversibility condition and its admissible space, the evolution of damage, for a given displacement $\mathbf{u}$, follows from the partial minimization of the total energy $E_{l_0}(\mathbf{u}, d)$ with respect to d:

$$E_{\mathrm{el}}(\mathbf{u}, d) + E_{\mathrm{frac}}(\mathbf{u}, d) \leq E_{\mathrm{el}}(\mathbf{u}, \hat{d}) + E_{\mathrm{frac}}(\mathbf{u}, \hat{d}) \quad \forall \hat{d} \in \mathcal{D}(d), \tag{9}$$

with $E_{\mathrm{el}}(\mathbf{u}, d) = \int_\Omega g(d)\Psi(\boldsymbol{\varepsilon}(\mathbf{u}))\, dV$.

2.2. Separation of tension and compression

The original formulations in Eq. (1) and (2) do not distinguish between the contribution of tension and compression in the energy available to propagate cracks. As a result, cracks may appear in compressive regions, and interpenetration of crack faces is not prevented. A modification of the elastic energy, which splits the strain energy into contributions from tension and compression, was proposed in [42]:

$$E_{\mathrm{ela.}} = \int_\Omega \left(g(d)\Psi^+(\boldsymbol{\varepsilon}) + \Psi^-(\boldsymbol{\varepsilon}) \right) d\Omega \tag{10}$$

Here, the strain energy density is decomposed into contributions from shear and positive volumetric changes, and from negative volumetric changes:

$$\psi^+(\boldsymbol{\varepsilon}) = \frac{1}{2}\kappa\langle \mathrm{tr}\boldsymbol{\varepsilon}\rangle_+^2 + \mu\boldsymbol{\varepsilon}^{dev} : \boldsymbol{\varepsilon}^{dev}, \qquad \psi^-(\boldsymbol{\varepsilon}) = \frac{1}{2}\kappa\langle \mathrm{tr}\boldsymbol{\varepsilon}\rangle_-^2. \tag{11}$$

Other splitting strategies have been proposed, such as the spectral split [43] and the alternative decomposition presented in [44]. The importance of separating tension and compression will be discussed in the outlook section of the article, in particular the incompatibility of energy decomposition with the formulation introduced in the next Section. The fragmentation case presented in this work, as well as classical expanding rings and shells experiments [7,45], are mainly driven by tension. When using the AT1 model with an elastic threshold, we expect the influence of the energy split to be negligible in the non-degraded case. Cohesive element simulations of the Mott expanding ring case confirm that the resulting fragment mass distributions is correctly captured with purely tensile cohesive fracture [46]. Therefore, we do not use the energy split in the simulation results presented in this work. This stance is valid for the present study, but does not translate for general fragmentation cases where compression is not negligible, such as during an impact.

2.3. Mass degradation

The degradation of stiffness in Eq. (2) is accompanied by a corresponding reduction of the elastic wave speed in the damaged zone:

$$c_s = \sqrt{\frac{g(d)\mu}{\rho}}. \tag{12}$$

An interesting approach, which does not lead to this alteration of the wave velocity, is proposed in Ref. [47,48]. The authors of these works argue that fracture is not necessarily associated with a loss of elastic wave velocity in the process zone, and suggest a strategy to preserve it by scaling the mass density in the same way as the stiffness. If the stiffness is scaled by the degradation function $g(d)$, the mass density is similarly scaled as $\rho(d) = g(d)\rho_0$.

This ensures that the elastic wave velocity in the process zone remains constant. For example, the shear wave speed c_s satisfies

$$c_{pz} = \sqrt{\frac{\mu(d)}{\rho(d)}} = \sqrt{\frac{\mu_0\, g(d)}{\rho_0\, g(d)}} = c_s. \tag{13}$$

Naturally, this procedure leads to a process called mass erosion, and does not satisfy the general principle of mass conservation.

The complete energy functional with this addition would be

$$E_{l_0}(\mathbf{u}, d) = \int_\Omega g(d)\Psi(\boldsymbol{\varepsilon}(\mathbf{u}))\, dV + \frac{G_c}{c_w}\int_\Omega \left(\frac{w(d)}{l_0} + l_0 \|\nabla d\|^2 \right) dV - \int_\Omega \frac{1}{2} g(d)\rho\dot{\mathbf{u}}\cdot\dot{\mathbf{u}}\, dV - W_{\mathrm{ext}}(\mathbf{u}), \tag{14}$$

whose derivative with respect to d would give a contribution of the kinetic energy. While a formal adherence to the variational formulation requires including this term in the damage problem, its justification remains purely mathematical. In the context of this study, mass degradation is primarily employed to preserve wave velocity within damaged regions. Incorporating the damage contribution to mass density solely in the dynamic problem is sufficient for this purpose, and extending this contribution to the phase-field evolution lacks physical motivation. Therefore, the damage problem formulation remains unchanged throughout this work.

2.4. Numerical implementation

The problem is discretized using the finite element method and is implemented in the open-source FEM library Akantu [49]. The implementation is largely based on [36]. Given a mesh discretization Ω_h of the domain Ω, the quantities of interest are interpolated inside any element $\Omega_e \in \Omega_h$ by

$$\mathbf{u}(\mathbf{x}) = \mathbf{N}(\mathbf{x})\underline{\mathbf{u}}^e, \qquad \boldsymbol{\varepsilon}(\mathbf{u})(\mathbf{x}) = \mathbf{B}(\mathbf{x})\underline{\mathbf{u}}^e, \tag{15}$$

$$d(\mathbf{x}) = \mathbf{N}_d(\mathbf{x})\underline{\mathbf{d}}^e, \qquad \nabla d(\mathbf{x}) = \mathbf{B}_d(\mathbf{x})\underline{\mathbf{d}}^e, \tag{16}$$

with $\mathbf{N}$ and $\mathbf{B}$ the interpolation and differentiation matrices. $\underline{\mathbf{u}}^e$ and $\underline{\mathbf{d}}^e$ are the nodal values of the displacement and damage on the element Ω_e.

Rather than using a monolithic approach, the dynamic problem and the damage problem are solved in a staggered manner.

As the overall goal of this project is to investigate large-scale fragmentation problems, explicit time integration becomes advantageous due to its computational efficiency and amenability to parallelization. Similarly, linear triangular elements are chosen here for their low computational cost. Hence, the displacement $\mathbf{u}$, velocity $\dot{\mathbf{u}}$ and acceleration $\ddot{\mathbf{u}}$, satisfying the damage-dependent elastodynamic equilibrium, are updated using an explicit Newmark scheme:

- From a step n corresponding to an arbitrary time t, a predictor step computes the displacement and parts of the velocity at time $t + \Delta t$,

$$\underline{\mathbf{u}}_{n+1} = \underline{\mathbf{u}}_n + \Delta t\underline{\dot{\mathbf{u}}}_n + \frac{\Delta t^2}{2}\underline{\ddot{\mathbf{u}}}_n, \tag{17}$$

$$\underline{\dot{\mathbf{u}}}^P_{n+1} = \underline{\dot{\mathbf{u}}}_n + \frac{\Delta t}{2}\underline{\ddot{\mathbf{u}}}_n. \tag{18}$$

- The computation of the acceleration increment comes from the weak form of Eq. 7

$$\mathbf{M}\delta\underline{\ddot{\mathbf{u}}} = \mathbf{F}_{\text{ext}} - \mathbf{F}_{\text{int}} - \mathbf{M}\underline{\ddot{\mathbf{u}}}_n. \tag{19}$$

  The external force $\mathbf{F}_{\text{ext}}$ is assembled from the surface traction $\mathbf{f}$ and potential body force $\mathbf{b}$, while the internal force $\mathbf{F}_{\text{int}}$ is assembled from the elementary vectors $\mathbf{F}^e_{\text{int}} = \int_{\Omega^e} \mathbf{B}\sigma(\mathbf{B}\underline{\mathbf{u}}^e, \mathbf{N}_d\underline{\mathbf{d}}^e)\, dV$.
- A corrector step updates the velocity and acceleration

$$\underline{\ddot{\mathbf{u}}}_{n+1} = \underline{\ddot{\mathbf{u}}}_n + \delta\underline{\ddot{\mathbf{u}}}, \tag{20}$$

$$\underline{\dot{\mathbf{u}}}_{n+1} = \underline{\dot{\mathbf{u}}}^P_{n+1} + \frac{\Delta t}{2}\underline{\ddot{\mathbf{u}}}_{n+1}. \tag{21}$$

The damage problem is solved once per time step using the current displacement field. The phase-field equation is obtained from the minimization of the energy functional with respect to the damage variable d, Eq. (9). Its weak form, with AT1 formulation, reads: Find $d \in [0, 1]$ such that

$$\int_\Omega \left(-2(1-d)\Psi(\boldsymbol{\varepsilon}(\mathbf{u}))v + \frac{3G_c}{8}\left(\frac{1}{l_0}v + 2l_0\nabla d \cdot \nabla v\right)\right) dV = 0. \quad \forall v \in [0, 1] \tag{22}$$

The subsequent finite element discretization leads to the following element-level contributions to the Hessian matrix H and the residual vector b:

$$\mathbf{H}^e = \int_{\Omega^e} \left(2\Psi(\mathbf{B}\underline{\mathbf{u}}^e)\mathbf{N}_d^T\mathbf{N}_d + \frac{3G_c}{8}l_0\mathbf{B}_d^T\mathbf{B}_d\right) dV, \tag{23}$$

$$\mathbf{b}^e = \int_{\Omega^e} \left(2\Psi(\mathbf{B}\underline{\mathbf{u}}^e) - \frac{3G_c}{8l_0}\right)\mathbf{N}_d\, dV. \tag{24}$$

Following [36] again, the damage problem can be reformulated as a bound-constrained quadratic optimization problem:

$$\min_d \quad \frac{1}{2}d^T H d - d^T b \quad \text{s.t.} \quad 1 \geq d \geq d_n, \tag{25}$$

where the box constraint $1 \geq d \geq d_n$ enforces the damage irreversibility.

This problem is solved using the Gradient Projection Conjugate Gradient (GPCG) method, as implemented in the Toolkit for Advanced Optimization (TAO) of the PETSc library [50–52]. PETSc is an MPI-based library providing routines and data structures for the scalable, parallel solution of large-scale partial differential equations. Within this framework, TAO provides algorithms for large-scale optimization, including GPCG. GPCG is an algorithm to solve bound constrained quadratic optimization problems. It utilizes a Gradient Projection strategy to identify a face to explore, with active variables currently at a boundary. The active variables are then fixed and a Conjugate Gradient method is used to explore the face with the remaining free variables. The algorithm then switches back to the projection phase to identify a new face to explore until a satisfying approximation of the solution is found. More details on this method can be found in Ref. [53].

Both the dynamic and the damage models are parallelized in Akantu using a ghost element strategy, more details on its implementation can be found in Ref. [20,54].

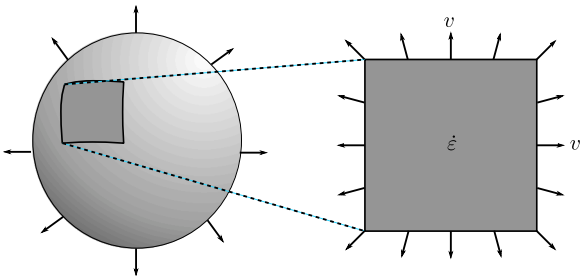

Fig. 2. Geometry and boundary conditions for the fragmentation of an expanding spherical membrane, and the equivalent 2D problem, a plate in radial expansion.

3. Dynamic fragmentation and damage spreading

As an initial demonstration of dynamic fragmentation, and to illustrate the difficulties that arise when using the classical phase-field formulation without mass degradation, we consider the case of an expanding spherical membrane, pictured in Fig. 2. A square portion of the sphere, of size 1 cm × 1 cm, is extracted and approximated in two dimensions as a square plate in plane-strain condition and subjected to radial loading. The geometry is discretized using 195,332 linear triangular elements.

A velocity gradient is prescribed throughout the domain to impose a uniform initial strain rate $\dot{\epsilon}$ at the beginning of the simulation. This loading is then maintained by incrementally adjusting the imposed displacement at the boundary to preserve the target strain rate during the dynamic evolution.

The material parameters are: a Young's modulus $E = 370\,\text{GPa}$, a Poisson's ratio $\nu = 0.22$, and a density $\rho = 3900\,\text{kg m}^{-3}$. The regularization length is set to $l_0 = 0.111\,\text{mm}$. The critical energy release rate G_c is modelled via a Weibull distribution with probability density function

$$f(x;\lambda,k) = \begin{cases} \frac{k}{\lambda}\left(\frac{x}{\lambda}\right)^{k-1} e^{-(x/\lambda)^k}, & x \geq 0, \\ 0, & x < 0, \end{cases} \tag{26}$$

with the scale parameter $\lambda = 50$ and the shape parameter $k = 10$ to account for material heterogeneity. These parameters yield a mean $\bar{G}_c = 47.6\,\text{J m}^{-2}$ and a standard deviation of $5.7\,\text{J m}^{-2}$.

As explained in the previous section, the problem is solved using an explicit Newmark scheme with a time step $\Delta t = 3.367 \times 10^{-3}\,\text{ns}$ and the damage problem being solved at each time step.

The crack pattern obtained for a strain rate of $\dot{\epsilon} = 100\,\text{s}^{-1}$ and at four different times is shown in Figs. 3a-3d. We observe the nucleation, propagation, and coalescence of multiple fractures, ultimately leading to the formation of fragments. However, the crack propagation is accompanied by a substantial widening of the damage bands, reaching several times their initial width. As a result, the behaviour within the damaged zones becomes difficult to interpret, and the precise geometry of the resulting fragments cannot be reliably determined. Furthermore, a significant fraction of material is effectively lost within these highly damaged regions, which may compromise the accuracy of the predicted fragment masses. The majority of the crack width consists of highly damaged material. Specifically, 20.0 % of the total plate surface exhibits a damage level of $d \geq 0.9$. Under these conditions, the test yields 27 fragments.

Employing an energy decomposition yields a similar widening of the damage bands, as shown in Appendix A.

The next sections investigate the mechanisms responsible for this excessive increase in crack thickness and explore the use of mass degradation as a strategy to obtain qualitatively more interpretable results in dynamic fragmentation. To illustrate our purpose, the same simulation test is now repeated with mass degradation. The resulting crack pattern is shown in Figs. 3e-3h. As observed, the widths of the damage bands are better controlled, allowing the shapes of the resulting fragments to be identified with greater accuracy. In contrast to the non-degraded case, only 6.4 % of the surface area is damaged above $d = 0.9$, despite producing a higher count of 30 fragments.

4. Interaction of elastic waves with damage

4.1. Wave reflection at a damaged free boundary

The objective of this section is to compare the behaviour of a free boundary with that of a damaged boundary under dynamic loading. To investigate the reason for the observed widening of the damage bands, we simplify the problem to a pseudo-1D bar, illustrated in Fig. 4.

The bar, of length $L = 5\,\text{mm}$, is discretized using linear triangular elements of base and height $h = 5\,\mu\text{m}$, which is also the height of the bar. For the material parameters, we choose a Young's modulus $E = 275\,\text{GPa}$, a Poisson's ratio $\nu = 0$, and a density of $\rho = 2750\,\text{kg m}^{-3}$. The fracture related parameters are $G_c = 200\,\text{J m}^{-2}$ and $l_0 = 200\,\mu\text{m}$, which is much larger than the mesh size and ensures a good resolution of the response within the damaged region. The right end of the bar is left free to undergo horizontal motion.

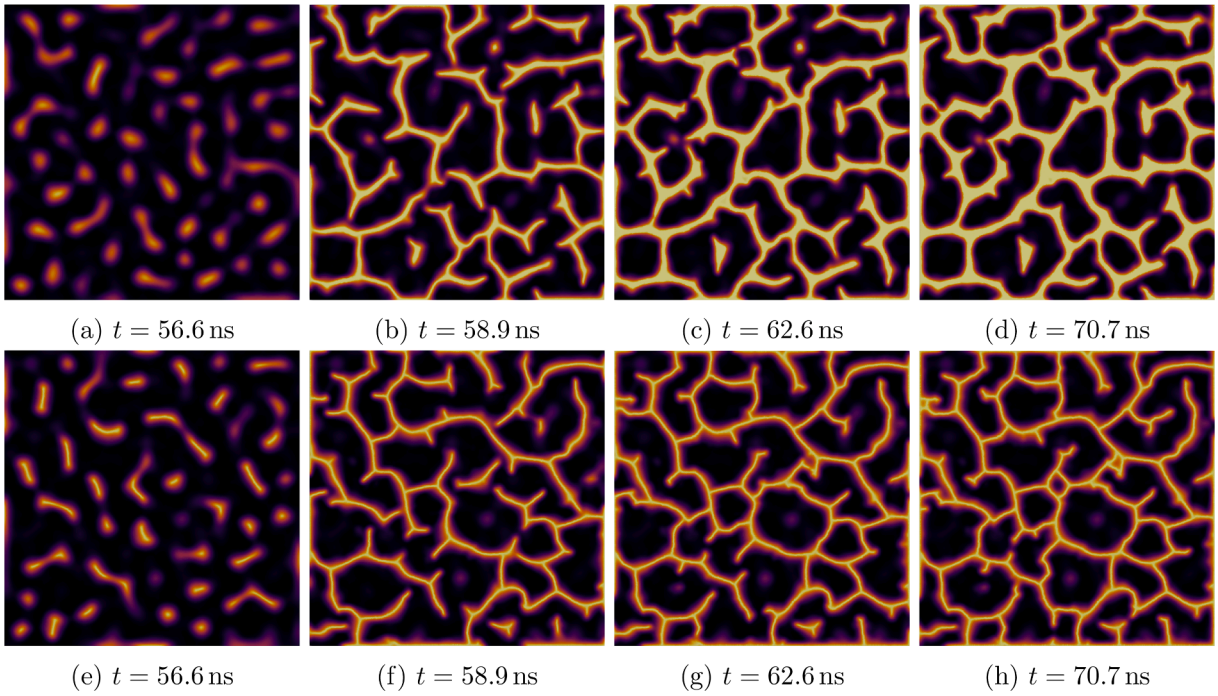

Fig. 3. (a)-(d) Damage field without mass degradation at four different time steps. (e)-(h) Damage field with mass degradation at four different time steps.

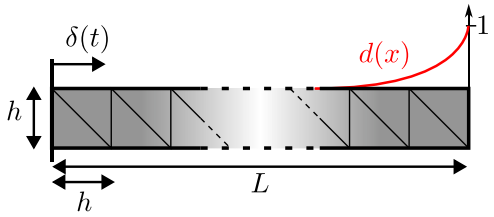

Fig. 4. Geometry and boundary condition of the 1D bar test. An impulse is sent from the left toward a free boundary (right), with or without damage.

Damage is prescribed to be equal to 1 at the right boundary, and the corresponding optimal damage profile is obtained by solving the damage problem. A sinusoidal impulse $\delta(t) = 0.08\frac{E}{\rho}\Delta t \sin\frac{\pi t}{1200\Delta t}$ is applied at the left end of the pseudo-1D bar for the 600 first time steps, as shown in Fig. 4. The amplitude of the impulse is chosen sufficiently small to prevent the nucleation of additional damage. The subsequent dynamic simulation is carried out using the same explicit time-integration scheme, with a time step $\Delta t = 96.65\,\mathrm{ns}$ for the solid model, while the damage field is still updated at each step to ensure that no damage develops in the intact part.

A reference simulation is first conducted without damage to establish a baseline for the subsequent analysis. The results are presented in Fig. 5 as a c-t diagram showing the strain as a function of time and of the position along the bar, normalized by the regularization length. The compressive wave propagates from the left boundary toward the right. As expected, upon reaching the free end, the incident compressive wave is sharply reflected as a tensile wave, producing a clear change of sign in the strain field. A small amount of numerical noise (dispersion) is visible after the passage of the impulse, but it does not affect the overall behaviour of the solution. This can also be seen in Fig. 6, which shows the strain as a function of position at three different times. The reflected wave maintains its shape and amplitude, and the noise remains of small amplitude after the main wave passes.

The simulation is then repeated with a damaged boundary, first without mass degradation, as shown in Fig. 7. The same impulse propagates from the left toward the right. Upon reaching the damaged end, the wave is progressively slowed down and the strain amplitude increases by several orders of magnitude. A portion of the wave is reflected earlier than in the reference case, indicating a modification of the effective boundary response. Following the arrival of the wave, the damaged region enters what may be described as a ringing regime: waves become trapped within the damaged zone, and small oscillations persist over time. The damaged end continues to emit alternating tensile and compressive waves, which subsequently interact with the next incoming main wave. Thus, even in the absence of additional damage spreading, the behaviour of the damaged boundary is problematic, as it does not reproduce the expected response of a free boundary.

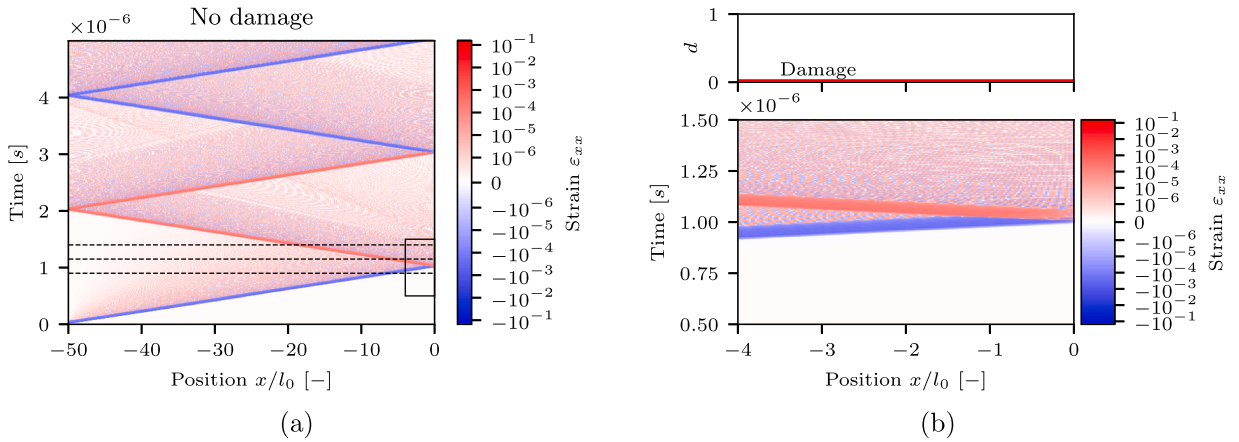

Fig. 5. (a) c-t diagram of the reference case without damage and (b) close up on the highlighted rectangular area. We observe a sharp reflection of the wave at the free boundary with a change of sign.

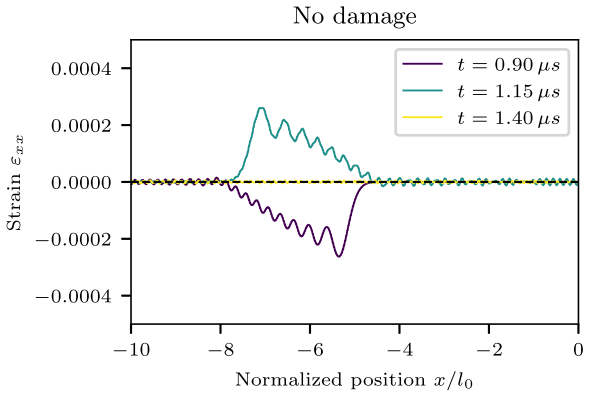

Fig. 6. Strain as a function of the position close to the free boundary for the reference case without damage at three different times marked by dashed lines in Fig. 5a.

The simulation is again repeated with mass degradation, as shown in Fig. 8. In this case, a sharp reflection is recovered, much closer to the reference free-boundary response. The wave is no longer slowed down, as the wave velocity is preserved within the damaged zone, and little to no increase in strain amplitude is observed. Fig. 9 shows the strain as a function of position at three different times, respectively without and with mass degradation. The deformation of the reflected wave can clearly be seen in the first case, along with the presence of residual oscillations after the main wave passage. The right part of the figure shows a shape of the reflected wave much closer to the original impulse. The behaviour with loss of mass is not entirely ideal, however: a small portion of the reflected wave does not undergo a complete sign reversal, and the reflection still occurs slightly earlier than expected. Nevertheless, these results demonstrate that preserving the wave speed within the damaged region is essential for damage to accurately approximate a free boundary, thereby providing a more physically consistent representation of a fracture.

Complementing the present results, an analysis of the convergence of both models (with and without mass erosion) toward the reference result without damage is presented in Appendix B.

4.2. *Damage spreading mechanism*

We now investigate the damage spreading mechanism by considering the oscillations of a bar released from an initially compressed state. The configuration is analogous to the one introduced in Section 4.1 in terms of geometry and mesh size. The material parameters are identical to those used in the previous section, except for the regularization length, which is decreased to $l_0 = 20\,\mu$m, a value still larger than the mesh size. The bar is initially compressed from both ends by imposing a displacement $\delta = 15\,\mu$m.

After applying the imposed displacement, we first solve the problem with a single static step without damage to obtain the stress and displacement fields in the bar. The two ends of the bar are then released, and the system is free to evolve dynamically via the same explicit scheme with a time step $\Delta t = 96.65$ ns. Two release waves propagate from the ends of the bar and superpose at the centre where they reach a sufficient deformation to nucleate a crack and the simulation is continued for a few oscillations. This test is performed twice, first without and then with mass degradation Fig. 10.

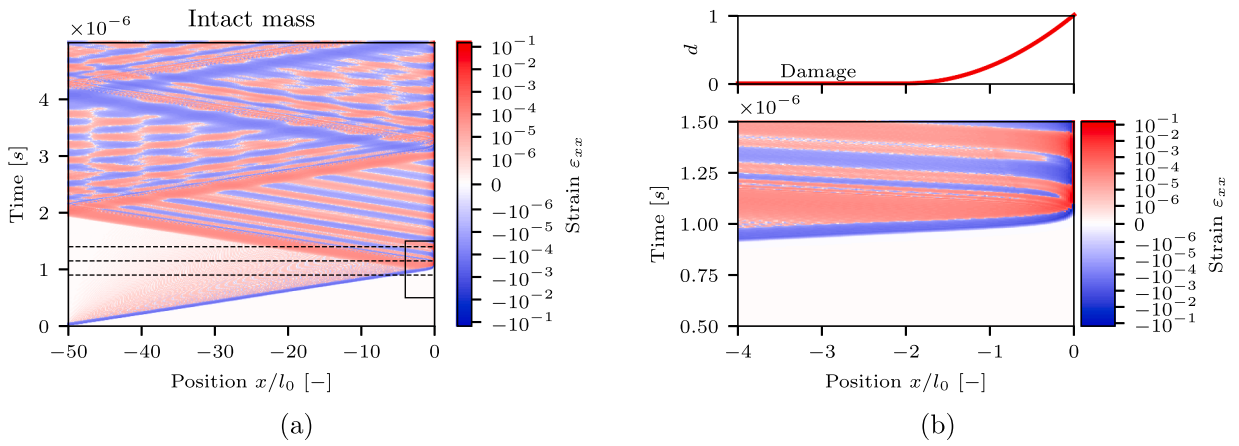

Fig. 7. (a) c-t diagram with damage but without mass degradation and (b)magnification on one reflection at the damaged end with the corresponding damage value. The reflection is not sharp any more and parts of the waves are trapped in the damaged area.

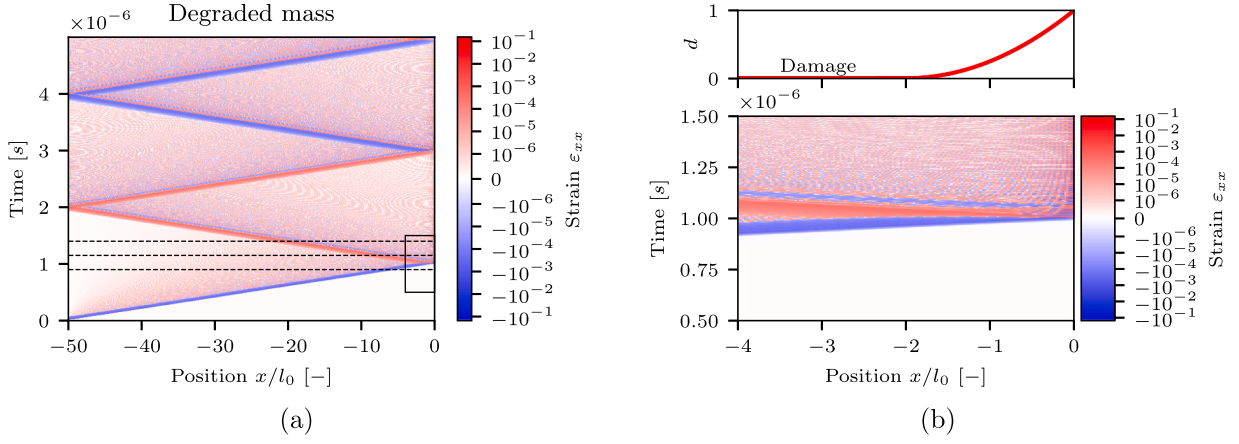

Fig. 8. (a) c-t diagram with damage and mass degradation and (b) magnification on one reflection at the damaged end. A sharp reflection is recovered, closer to the reference case. Note that the reflection is not perfect, as a part of the reflected wave does not change sign.

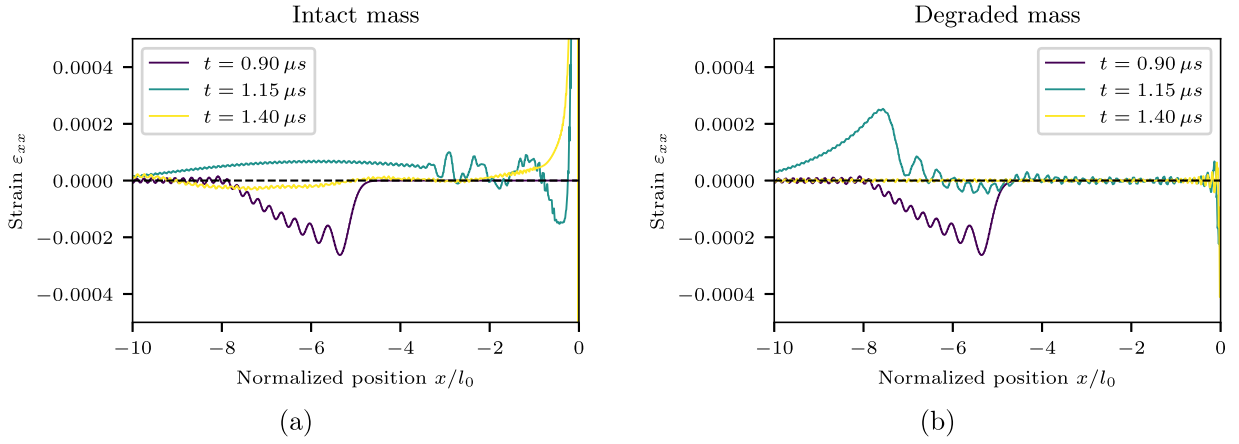

Fig. 9. Strain as a function of the position close to the damaged boundary for the three different times marked by dashed lines in Figs. 7a and 8a, (a) without mass degradation and (b) with mass degradation.

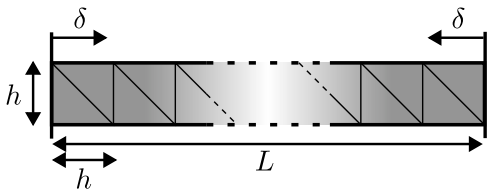

Fig. 10. Geometry and boundary conditions for the oscillation test.

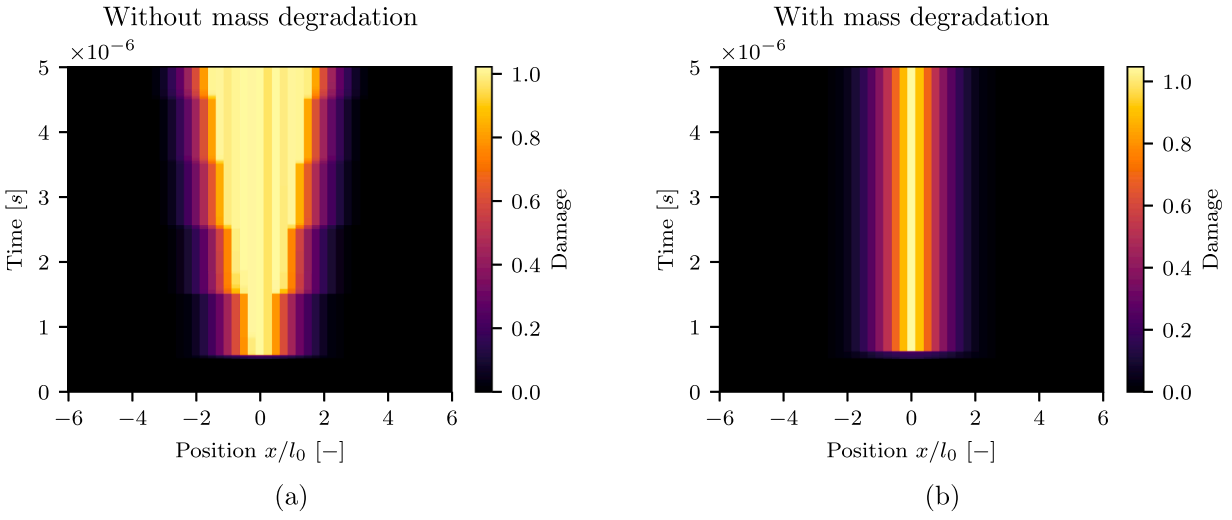

Fig. 11. c-t diagram of the damage as a function of time and position around the centre of the bar. (a) Without mass degradation an increase in damage with each incoming wave is observed, while (b) with mass degradation a stable damage profile is maintained.

Fig. 11 presents the results in the form of a c-t diagram. The heatmap displays the damage field as a function of time and position, normalized by the regularization length l_0. The view is restricted to the central region of the bar, where wave superposition occurs, and damage nucleation takes place. In both simulations, damage initiates when the first waves reach the centre, with an initial width close to the theoretical value of $4l_0$. In the case without mass degradation (left), each subsequent oscillation leads to a progressive increase in damage. It should be noted that a comparable expansion of the fracture zone occurs when employing an energy decomposition scheme, as reported in Appendix A. The tensile component of the wave interacts with the existing damage in a manner consistent with the observations detailed in the preceding section. In contrast, the case with mass degradation (right) exhibits a stable damage profile throughout the simulation.

This behaviour is further illustrated in Fig. 12, which shows the evolution of the elastic, kinetic, and dissipated energy over time. Both simulations begin with a conversion of elastic to kinetic energy as the bar is released. Upon arrival of the waves at the centre of the bar, damage nucleates and the dissipated energy increases. This event coincides with a reduction in kinetic energy and a corresponding rise in elastic energy due to wave reflection. The kinetic energy remains higher in the simulation without mass degradation. This can be attributed to a cleaner reflection of the wave in the simulation with mass degradation, in contrast to the perturbations present in the damaged zone in the first case. As expected, the simulation without mass degradation exhibits an incremental increase in dissipated energy with each oscillation.

Fig. 13 presents the c-t diagram of the strain along the entire length of the bar for both simulations. In both cases, the initially compressed bar relaxes as the release waves propagate from the ends toward the centre. Subsequently, the bar oscillates, with alternating tensile and compressive waves reflecting at the centre and at the boundaries.

In the simulation without mass degradation, the strain values in the middle of the bar reach higher amplitudes (with an absolute maximum for $\varepsilon_{xx} = 0.9$ versus $\varepsilon_{xx} = 0.29$ with mass degradation), and more damage develops during the early stages. As a result, more energy is trapped in the damaged zone and less of the waves are effectively reflected, leading to a thinner spatial span of the wave patterns. Moreover, the region of high strain grows over time when mass degradation is not applied.

A close up on a pair of reflected waves is shown in Fig. 14. With mass degradation, the transition from compression to tension remains smooth as the waves propagate through the damaged zone. Without mass degradation, however, the strain increases in the damaged region. This elevated strain promotes additional damage, as evidenced by the earlier outward movement of the $d = 0.5$ isoline, pushing in turn the higher and lower damage valued zones outward.

These findings indicate that when mass is preserved while the wave speed is reduced, elastic waves interact with the damaged zone in an undesirable manner.

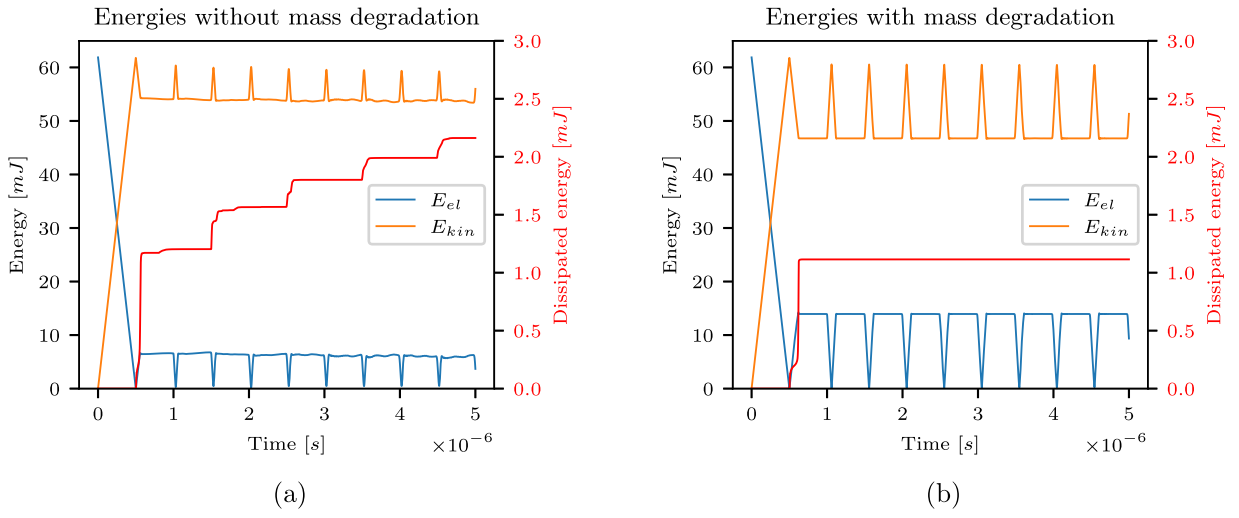

Fig. 12. Evolution of the elastic, kinetic and dissipated energy as a function of time for the oscillation test. (a) The plot for the simulation without mass degradation shows the increase in dissipated energy corresponding to the widening of the damage band. (b) With mass degradation, the dissipated energy reaches a steady state.

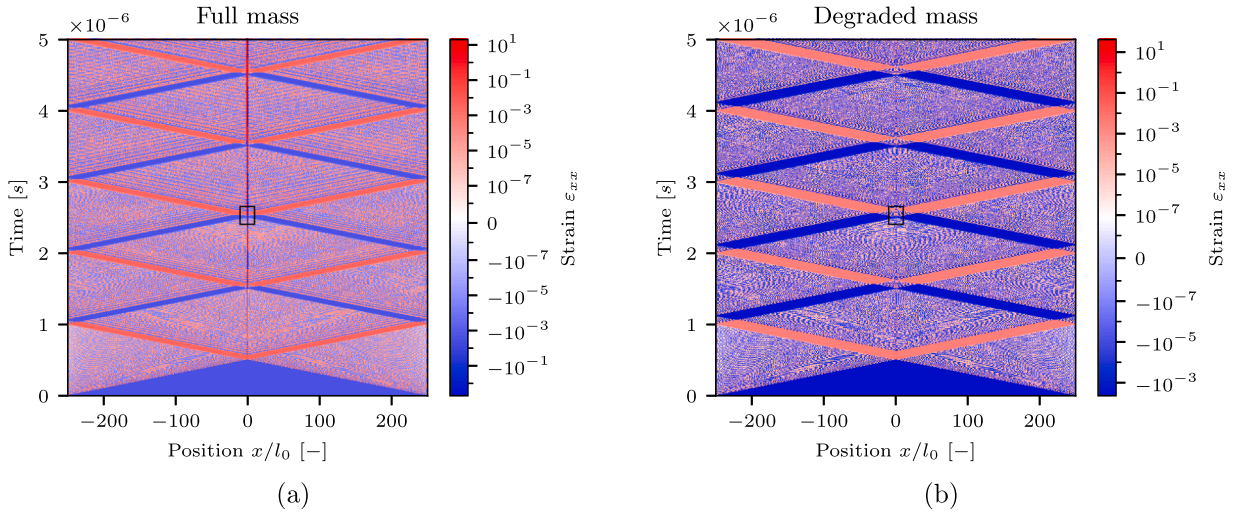

Fig. 13. c-t diagram of the strain in the whole bar length. (a) The case without mass degradation shows a shorter wave span tha (b) the case with mass degradation. A high strain area appears around the centre, corresponding to the damaged zone. This area increases over time in (a). Note the difference in scale for the compressive values. The magnification windows in black are shown in the next figure.

5. 2D Crack propagation and branching

5.1. Single crack dynamics

In the previous section, we identified the interaction of elastic waves with damage as a source of damage sprawl and other generally unwanted behaviour. We showed that preserving wave velocity is a key component for obtaining reliable results under high loading. We now shift to a two-dimensional setting to examine crack propagation with mass degradation.

We consider the example of a notched PMMA plate in 2D plane-stress condition, with the geometry and boundary conditions shown in Fig. 15a, following configurations similar to those in [55,56]. The material properties are $E = 3.09\,\text{GPa}$, $\nu = 0.35$, $G_c = 300\,\text{J}\,\text{m}^{-2}$, and $\rho = 1180\,\text{kg}\,\text{m}^{-3}$. The corresponding Rayleigh wave speed is $c_r = 906\,\text{m}\,\text{s}^{-1}$. A prescribed displacement Δu is imposed on the top and bottom boundaries of the plate.

As a first step, the solid mechanics problem is solved in a single static step without damage to obtain the stress and displacement fields throughout the domain. As before, the system is then allowed to evolve dynamically, with the damage field updated once per time step based on the current displacement state.

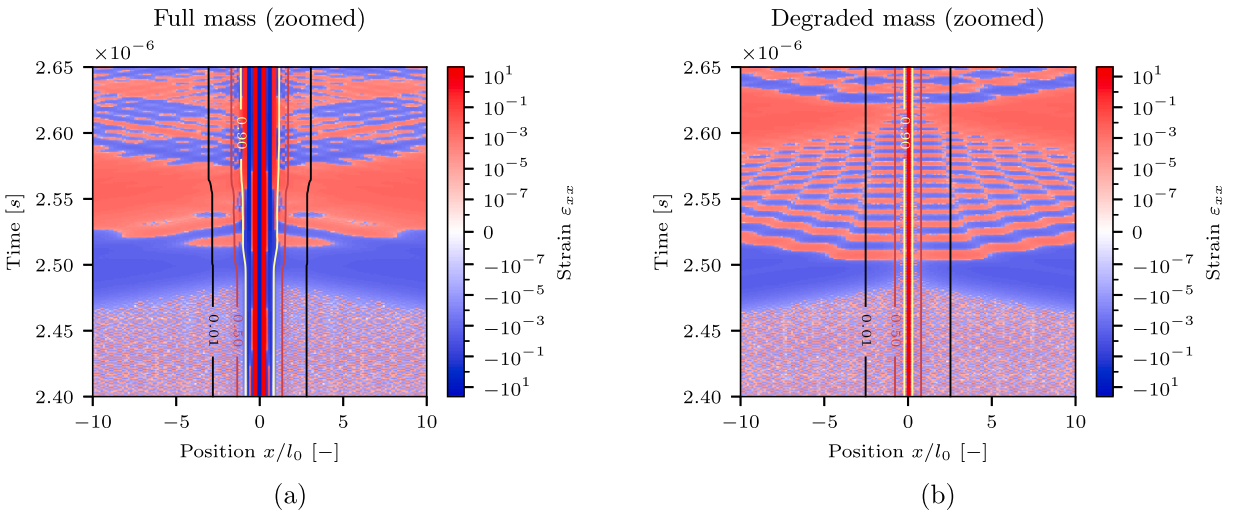

Fig. 14. Detail of the c-t diagram of the strain around the centre of the bar for one pair of reflected waves. The contour lines represent the damage levels $d = 0.01, d = 0.5$ and $d = 0.9$. (a) Without mass degradation, the value of the strain reach a high value associated with high damage. This zone of high strain grows as the waves are reflected. (b) With mass degradation, the zone of high strain value is also present but remains contained.

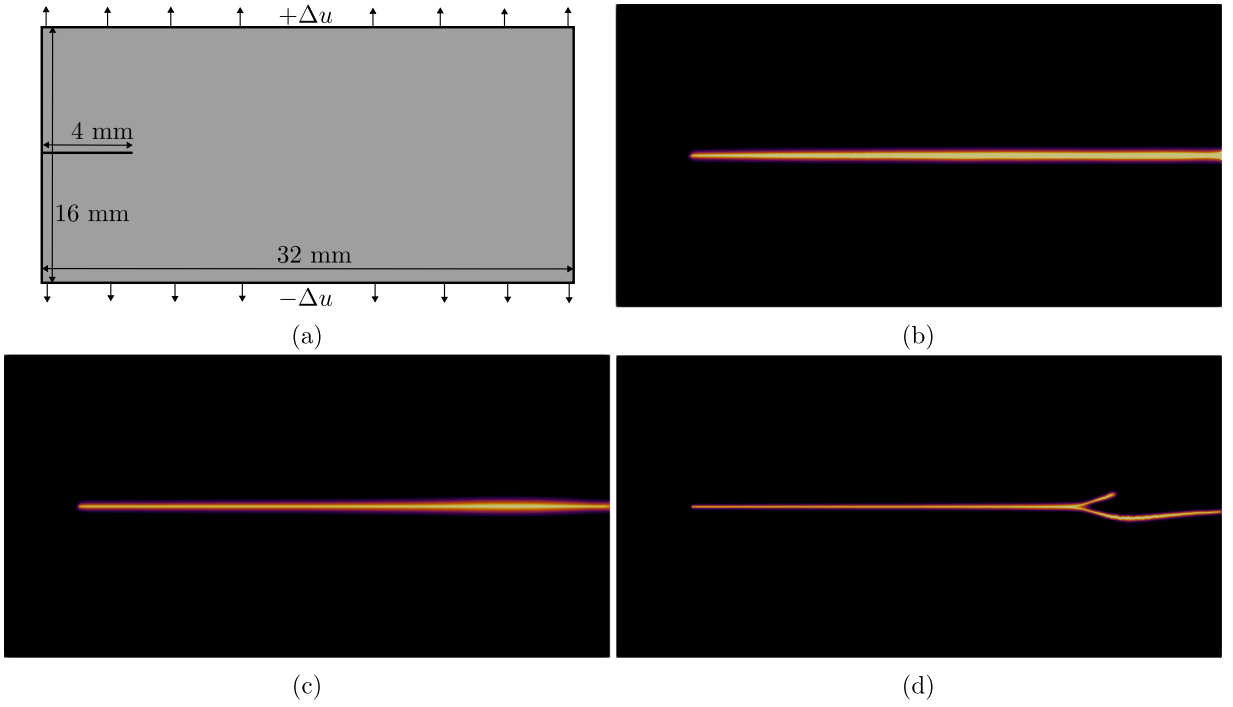

Fig. 15. (a)Geometry and boundary conditions for the crack propagation test. (b) Example of crack propagation at $l_0 = 0.2$mm and $\Delta u = 36\mu$m without mass degradation. The crack thickness increases as the crack advances and accelerates. (a) Crack propagation also at $l_0 = 0.2$mm and $\Delta u = 36\mu$m with mass degradation. The crack remains thinner than without mass degradation. (d) Crack propagation with mass erosion and a finer mesh, $l_0 = 0.1$mm and $\Delta u = 36\mu$m. The crack propagates and then branches.

An example of crack propagation without mass degradation is shown in Fig. 15b, for $l_0 = 0.2$ mm and $\Delta u = 36$ μm. The crack width increases rapidly as the crack accelerates, reaching values around twice its initial width-an effect already reported in [35,36]. No crack branching is observed in this case.

The same example, but with mass degradation, is shown in Fig. 15c. In this case, the crack thickness remains relatively low over more than half of its propagation path. It then widens before reaching the end of the plate, accompanied by an aborted branching attempt. Fig. 15d shows that, for a regularization length reduced to $l_0 = 0.1$ mm, branching is promoted and the wider crack near the

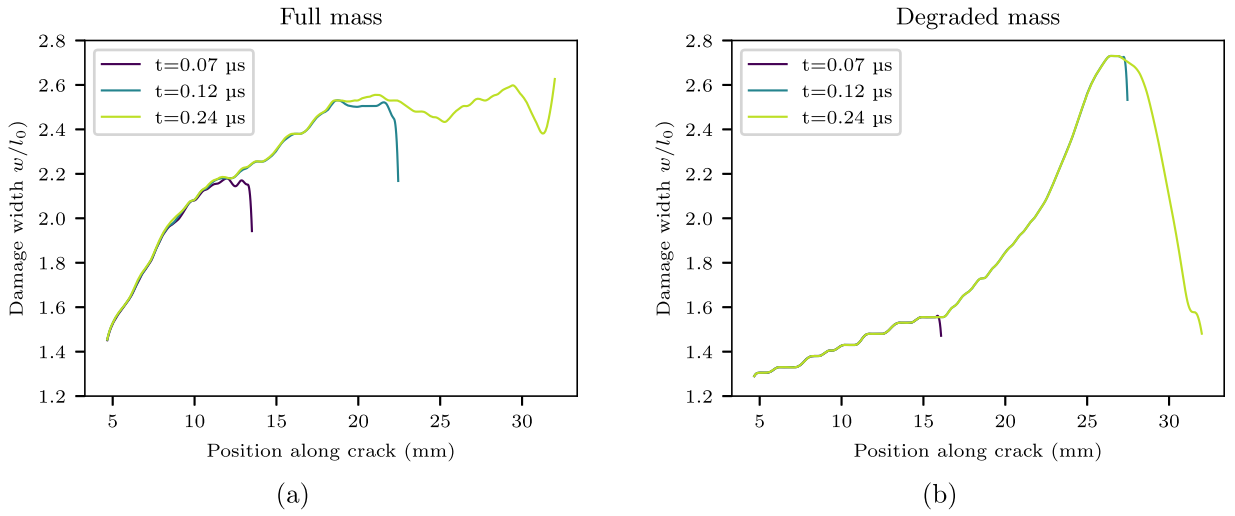

Fig. 16. Crack width along the crack paths in Figs. 15b and 15c for three different times, (a) with and (b) without mass degradation. The curves are superposed and damage does not evolve once it is set.

right end in Fig. 21b are now fully formed branches. As will be discussed in Section 5.2, branching occurs more readily when mass degradation is employed.

The crack thickness as a function of the crack length at different points in time is reported in Fig. 16. The crack width w is computed in post-processing by rasterizing the damage heatmap, thresholding at a certain damage value and counting the remaining pixel in each column. The difference in width lies primarily in the highly damaged area of the fracture, so a threshold of $d = 0.5$ is chosen. As the curves nearly superpose in time, and in opposition to the observations of the previous section, we conclude that no widening occurs after the passing of the crack. Vibrations and wave trapping are not significant in this simulation setup. Generally, the crack width is larger when there is no mass degradation. This can be imputed to slower unloading (slower wave speeds) of the fracture faces; the additional dissipation in the width of the crack is intimately linked to a slower propagation (see crack tip position as function of time).

A distinction should be made between the widening observed in 1D in the previous section, due to premature wave reflection in damaged zones, and the widening observed here, which is independent of wave interaction. While the former is non-physical and purely a numerical artifact, the latter has been proven to accurately represent the velocity toughening observed experimentally, as discussed in Ref. [55]. Although investigating the velocity toughening mechanism is beyond the scope of this work, it is interesting to note that while mass degradation limits fracture widening, this effect remains present, especially prior to branching.

The next step is to perform a convergence analysis of crack propagation as the regularization length l_0 tends to zero. The mesh element size h is refined accordingly such that

$$l_0 \to 0 \qquad \text{and} \qquad \frac{l_0}{h} \to \infty, \tag{27}$$

ensuring adequate resolution of the diffused crack as l_0 decreases. From this point onward, a fixed value for l_0 means also a corresponding fixed mesh size h whose values are displayed in the inset of Fig. 17. The boundary conditions remain the same as in Fig. 15. Convergence is assessed based on the crack-tip position as a function of time, the corresponding crack velocity, and the energy dissipation per unit crack extension.

The crack-tip position is defined as the rightmost point at which the damage variable satisfies $d \geq 0.9$. The crack velocity is computed by finite differences of the crack-tip position over successive time increments. The resulting velocity curves are subsequently smoothed using a moving-average filter.

Fig. 17 shows the crack-tip position as a function of time for decreasing values of the regularization length l_0, for both the cases with and without mass degradation. The simulations with mass degradation are shown using dashed lines. In both sets of curves, a darker colour corresponds to a smaller value of l_0. For the darkest dashed curves (smallest l_0), a kink appears in the trajectory. This kink corresponds to the onset of a branching event, as seen in Fig. 15d, which temporarily slows down the crack. A short delay before crack initiation is also noticeable, and this delay decreases as l_0 becomes smaller; more details on this phenomenon can be found in Ref. [57].

Remarkably, the simulations provide evidence of convergence of the phase-field approach, as the trajectories become closer to one another with l_0 decreasing. To the best of our knowledge, it is the first time that convergence is reported for a dynamically propagating crack. A second notable observation is the difference in slope between the two families of curves: the simulations with mass degradation exhibit a steeper slope, and therefore a higher crack velocity. The convergence trend is further reported in Fig. 18, where the distance between the crack tips of two consecutive decreasing regularisation lengths is presented at two different times in the simulation.

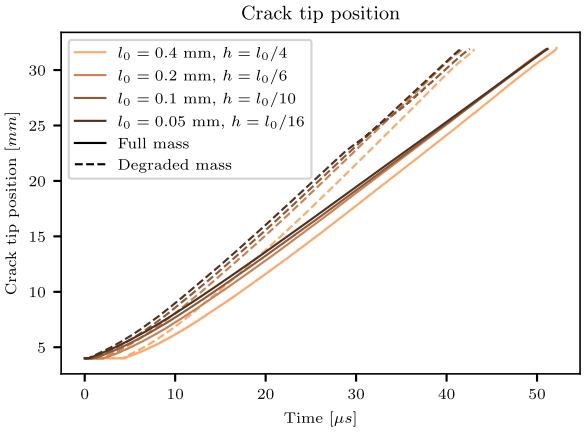

Fig. 17. Crack tip position as a function of time for decreasing regularization lengths l_0, for the case without mass degradation (full lines) and with mass degradation (dashed lines) and for an imposed displacement $\Delta u = 36\mu$m. The slopes of the curves are much steeper in the case with mass degradation. We observe a convergence as the regularization length decreases for both cases with and without mass degradation.

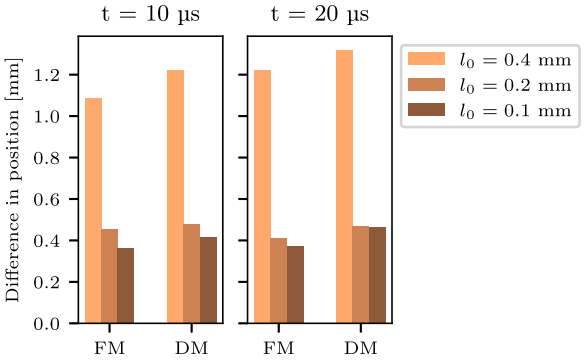

Fig. 18. Difference in position from Fig. 17 relative to the next lower l_0 value for two different times. FM is for full mass and DM for degraded mass. The difference in position decreases with l_0.

The corresponding crack velocities are reported in Fig. 19. Without mass degradation, the curves clearly converge to a steady velocity of approximately $0.6c_r$. When mass degradation is included, the fracture reaches higher velocities, exceeding $0.8c_r$, because the elastic waves are not slowed down in the process zone and less energy is dissipated within the crack width. The kink observed in Fig. 17 becomes even more pronounced here, as the velocity drops when the fracture begins to branch. This branching event also appears to occur earlier as l_0 decreases.

It is observed that the crack velocities obtained with mass degradation exceed the reported limiting velocity of $0.75c_r$ for PMMA [55, 56]. This discrepancy may be attributed to several factors. While the macroscopic toughness of PMMA is known to be rate dependent and crack propagation is not always accurately described by LEFM at high crack velocity [58], no rate-dependency is included in the present phase-field model. Nevertheless, momentary single-crack states, following the predicted crack velocity up to $0.9c_r$, have been observed between microbranching events [58]. Furthermore, crack velocities in brittle polyacrylamide gels have been shown to follow LEFM predictions before the appearance of instabilities above $0.87c_s$ [59], with c_s the shear wave speed of the material. While a comprehensive experimental validation remains beyond the scope of this study and further investigation into these effects is warranted, we consider the crack velocities reported here not to be in disagreement with experimental observations.

The dissipated energy is now examined in detail. The total dissipated energy is computed from the damage field using the Ambrosio-Tortorelli regularization,

$$E_d(d) = \frac{G_c}{c_w} \int_\Omega \left(\frac{w(d)}{l_0} + l_0 \|\nabla d\|^2 \right) dV, \tag{28}$$

and the dissipation rate is defined as the increment of dissipated energy per increment of crack length,

$$\Gamma = \frac{dE_d}{da} \tag{29}$$

with a denoting the theoretical crack length. Note that this method of computing is not accurate after branching, as the real crack length does not correspond to the computed value. The results are shown in Fig. 20.

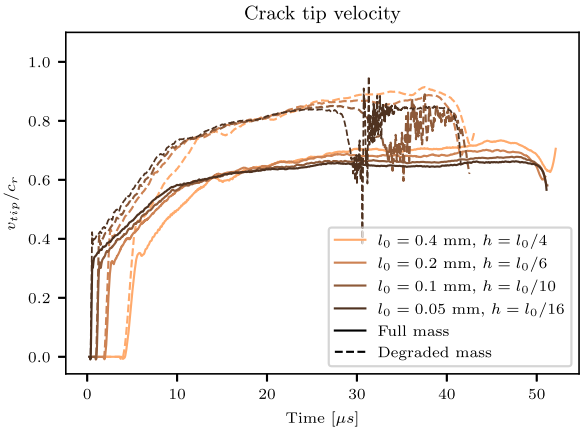

Fig. 19. Crack tip velocity as a function of time, normalized by c_r, for $\Delta u = 36\ \mu$m. Without mass degradation, the dynamically propagating cracks reach a velocity of approximately $0.6c_r$, while with mass degradation they reach a velocity of approximately $0.8c_r$.

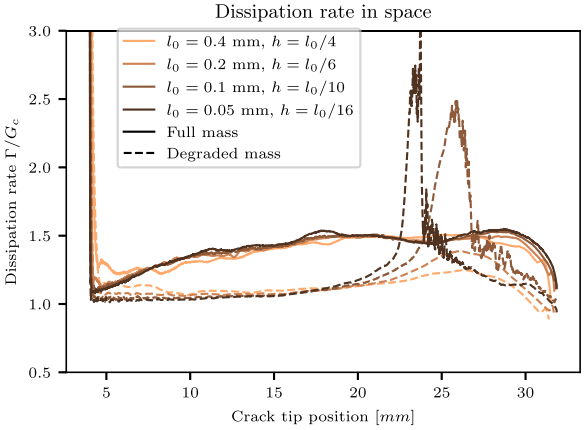

Fig. 20. Dissipation rate as a function of crack length, normalized by the critical energy release rate G_c, and for $\Delta u = \ \mu$m. The initial large value is an artifact at the onset of crack propagation, since the damage width increases without any crack advance. When the crack propagates, and in the case without mass degradation, the dissipation rate is higher than G_c. Degrading the mass leads to a dissipation rate converging to G_c. For a fine mesh, branching can be seen as the dissipation rate jumps to values larger than twice G_c.

The very large dissipation rate observed at the beginning of the simulation is an artifact due to the initial increase of damage near the notch tip, and hence dissipation, prior to the onset of crack propagation. Without mass degradation, once this initial transient has passed, the dissipation rate rises from $1G_c$ to slightly below $1.5G_c$. The lower crack velocity in this case leads to enhanced dissipation within the crack width.

With mass degradation, the dissipation rate converges toward G_c until the point at which branching initiates, at which point the dissipation goes above $2G_c$ for the two lowest regularization length. Again here, the lower rise in dissipation rate toward the end of the plate for the two lighter curves correspond to the widening of the crack observed in Fig. 15c, while the sharper peaks in the two darker curves correspond to the branching in Fig. 15d. The reduced dissipation rate favours branching, as the system seeks additional mechanisms to dissipate the required energy. The higher crack velocity in the degraded-mass case also makes the crack more susceptible to instabilities, either numerically in this case, or due to small material heterogeneities if they were included. Currently, it is unclear whether there can be numerical mesh convergence of dynamic instabilities such as branching events.

5.2. Branching crack dynamics

When examining branching behaviour, the contrast between the two formulations becomes particularly pronounced. Two examples of branching are shown in Figs. 21a and 21b, corresponding respectively to the cases without and with mass degradation. In this example, the regularization length is $l_0 = 0.1$ mm and the imposed displacement is $\Delta u = 45\ \mu$m.

In the absence of mass degradation, the fracture rapidly thickens, and significant instabilities develop before the first two branches finally separate. It is difficult to clearly characterize the sequence of events preceding branching, and small fragments appear immediately before the formation of the initial pair of branches. The crack then continues to propagate from one branch, alternately switching between the top and bottom branches as the other is aborted. A large, highly damaged region forms ahead of the crack tip

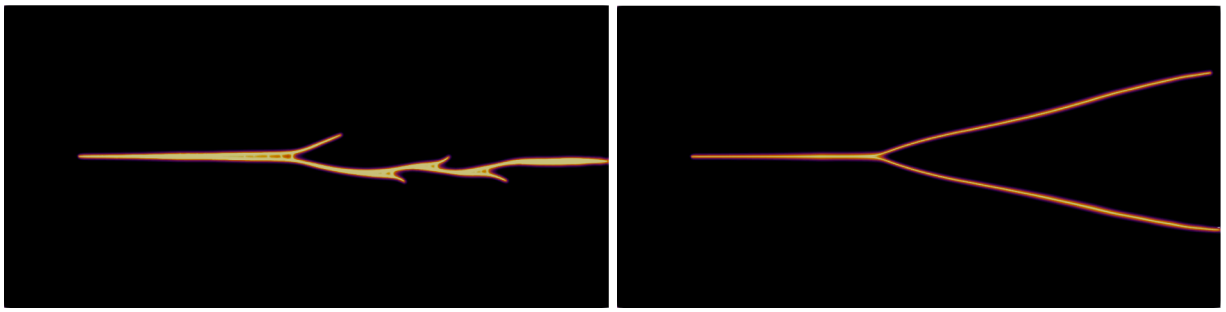

Fig. 21. Examples of branching for an imposed displacement of $\Delta u = 45\,\mu$m. (a) without mass degradation, the crack width is important prior to branching and the exact point at which it happens is hard to identify. (b) with mass degradation, the width of the crack stays controlled, and the branching is clearly defined.

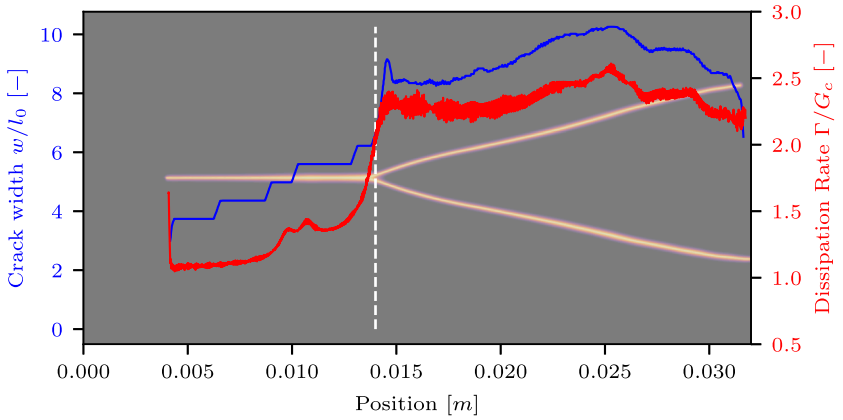

Fig. 22. Damage band width (in blue) and dissipated energy (in red) along the crack length. The branching is associated with a damage band width of twice its initial value and a dissipation rate of $2G_c$. (For interpretation of the references to colour in this figure legend, the reader is referred to the web version of this article.)

prior to each branching event. Although this effect may be less severe for moderate loading levels, it becomes increasingly problematic under extreme loading or fragmentation scenarios, where it is considerably amplified, as illustrated in Figs. 3a-3d.

In contrast, the corresponding simulation with mass degradation (Fig. 21b) exhibits a much more localized process, with the crack width remaining comparatively thin, aside from a slight widening observed before branching. The branching event itself is considerably more contained, and its initiation point can be identified with substantially greater precision. It is worth noting that the resulting branching pattern differs markedly from that obtained without mass degradation. Incidentally, a similar branching pattern can also be achieved without mass degradation by imposing a smaller displacement, Δu. In the non-degraded case, increasing Δu results in more chaotic branching and wider crack paths, whereas the mass-degraded formulation maintains a sharp, localized fracture geometry. While the physical relevance of this altered pattern lies beyond the scope of the present study, the key observation is that, when fragment identification is required, the mass-degraded formulation provides a more tractable and physically interpretable fracture geometry.

Fig. 22 shows the evolution of the thickness w of the crack along its path, along with the evolution of the dissipation rate Γ, calculated with Eqs. (28) and (29), for the case of mass degradation. The damage width w is computed the same way as in Fig. 16, but with a lower threshold of $d = 0.01$ to account for the whole width of the damage profile. The fracture energy and the crack width typically increase prior to branching [60,61], and a critical point is reached when the crack thickness exceeds twice its initial size, i.e. $8l_0$, and when the dissipation rate reaches $2G_c$ [55]. This remains true with mass degradation, but it is much more localized around the point of branching. Initially, the crack thickness is close to $4l_0$, consistently with the analytical prediction. It then gradually increases along the propagation path, with a marked acceleration shortly before the branching event, at which point the thickness exceeds $8l_0$. Beyond this threshold, the measured value of w remains high, as the thickness of both branches is included in the computation and no correction is applied for the propagation angle. The dissipation rate Γ exhibits a similar structure. Starting near G_c, it increases in two stages: a first rise corresponding to a widening of the crack, followed by a much sharper increase as the fracture begins to branch, ultimately exceeding $2G_c$.

These observations further demonstrate that preserving the wave velocity within the damaged zone is a key factor in limiting the widening of the damage band, thereby yielding more interpretable results in highly dynamic scenarios such as fragmentation. However, the intention is not to advocate the indiscriminate use of mass degradation as a universal remedy, as this approach introduces its own set of limitations.

6. Conclusion

Our simulation results reveal that the interactions between elastic waves and damage play a central role in the formation and growth of damage bands in phase-field modelling of dynamic fracture and fragmentation. In the standard phase-field formulation, stiffness degradation reduces the wave speed in the damaged regions. We have illustrated for an idealized 1D setting that part of the elastic waves are trapped in the damaged zones, which therefore do not behave appropriately as free boundaries. Crucially, elastic waves interacting with the damaged zone can induce additional damage, even when no further energy is supplied. In higher dimensions, for propagating cracks, the standard phase-field formulation leads to thick damage bands that dissipate energy above G_c and propagate at speeds slower than expected. All these problems are alleviated by preserving the wave speed through mass degradation. Our results show that damage bands yield sharper wave reflections and more stable damage behaviour.

Remarkably, our simulation results show encouraging numerical evidence, for a wide range of crack velocities, of convergence to Griffith and a well-defined fracture energy. For larger crack velocities, crack branching instabilities develop, and it is not yet clear what triggers those instabilities. Branches obtained with mass degradation are sharper and consistent with previously reported simulations results that show a dependence of branching on crack width and dissipation rate.

There are, however, several limitations to the mass-degradation approach, and we wish to stress that the primary aim of this paper is to explain the crack widening phenomenon rather than promoting this method. First, degrading the mass evidently violates both mass and energy conservation. In the experiment presented in Section 4.2, we have estimated the energy lost due to mass degradation to be around 0.1% of the internal energy in the system, a value that is comparable to the numerical error due to the integration scheme. In contrast, when more fractures are present, the amount of lost energy becomes non-negligible. It is the case, for instance, of the fragmentation case presented in Figs. 3e-3h, this loss rises to around 7% of the total energy injected in the system. Although this works against the use of this method, this aspect can be put into perspective with the amount of completely damaged material when no degradation of mass is employed. This damaged material contribute to the conservation of energy by holding kinetic energy, yet has no more physical effect on the rest of the system.

One of the other limitations of the implementation presented herein is its incompatibility with tension-compression energy splits: restoring stiffness in compression without restoring the corresponding mass results in a wave speed that tends toward infinity, which in turn leads to numerical instability in explicit time-integration schemes.

This problem could be resolved by introducing directional mass erosion, in which the degradation of inertia is linked to the deformation modes obtained from the decomposition of the strain field. For example, when stiffness degradation in many phase-field formulations is performed with respect to the eigenvalues and principal directions of the strain tensor (spectral split), a consistent strategy is to degrade the mass density according to the same modes. To achieve this, the strain field at the integration points is decomposed into its principal components, and the associated deformation modes are reconstructed at the nodal level by expressing the nodal displacements as functions of the strains.

The resulting modal displacements indicate how each degree of freedom contributes to tensile or compressive deformation. Mass degradation can then be applied only to the components associated with tensile modes by weighting the diagonal mass matrix according to the relative contribution of these displacement modes. Consequently, inertia is degraded only in directions contributing to tensile deformation, while compressive directions remain unaffected. Therefore, the assessment of directional mass degradation will be addressed in a future contribution.

We emphasize that the main benefit of mass degradation is that it yields qualitatively cleaner and more interpretable fragmentation patterns. We have argued that there are some experimental observations suggesting that wave speeds are preserved inside the process zone, but this assumption may not hold for all materials. In cases where the process zone contains microcracks, crushed material, or damaged fibres, the local microstructure may significantly alter wave propagation, and a constant wave speed may no longer be physically justified.

Nevertheless, it remains a valuable tool, as it provides a simple and powerful numerical technique to circumvent the enlargement of damage bands due to premature wave reflection within the damaged zones, provided that the influence of compression remains negligible. This method has been successfully employed in previous dynamic phase-field fracture simulations [47,48].

Other strategies could also be explored. For instance, one may adjust the degradation function applied to the mass, seeking a compromise that reduces the crack thickness while retaining some of the mass to limit the increase of wave speed when an energy split is used. Higher-order formulations can improve dynamic simulations by reducing localization errors [40] and have been used to model dynamic fragmentation [62]. In the current context, such models may not necessarily prevent the premature reflection of the elastic wave in damaged zones. Nonetheless, it remains to be determined whether improved localization yields better control over the widening of damage bands. Beyond elastic models, approaches based on plasticity offer an interesting alternative, particularly when the elastic stiffness is not degraded [63,64]. In addition, the yield stress in such models provides a critical stress that is independent of the regularization length, which helps conciliate the choice of a regularization length adapted to the desired resolution and a critical stress corresponding to the material of interest.

CRediT authorship contribution statement

Shad Durussel: Writing – review & editing, Writing – original draft, Visualization, Software, Methodology, Investigation, Funding acquisition, Formal analysis, Conceptualization; **Gergely Molnár:** Writing – review & editing, Methodology, Conceptualization; **Jean-François Molinari:** Writing – review & editing, Supervision, Project administration, Methodology, Funding acquisition, Conceptualization.

Data availability

Data will be made available on request.

Declaration of competing interest

The authors declare that they have no known competing financial interests or personal relationships that could have appeared to influence the work reported in this paper.

Acknowledgments

The authors wish to acknowledge Nicolas Richart and Guillaume Anciaux for their help in the implementation of the phase-field model and optimization solver. They also thank Laura De Lorenzis for the discussions on phase-field modelling and on implementation of the irreversibility of damage. This research received founding from the ESA OSIP Idea program, with contract number 4000144496.

Appendix A. Damage sprawl with energy decomposition

As discussed in the conclusion of this work, mass erosion is incompatible with energy decomposition. Therefore, it was not employed, ensuring consistency between the mass degradation and full mass scenarios. However, it should be noted that the issue of damage band widening persists when an energy decomposition strategy is used. As an example, we present results obtained with a volumetric-deviatoric split, as described in Eqs. 10 and 11.

Fig. A.23a illustrates the expansion of damage around the centre of the bar from Section 4.2, analogous to the results presented in Fig. 11a. Although the sprawl of damage is more contained than in cases without energy decomposition, since the compressive component of the strain energy does not contribute to damage evolution, an increase in damage is still observed as each wave arrives and reflects at the centre of the bar.

The crack pattern obtained from the radially loaded square plate experiment (Fig. 2) is reported in Fig. A.23b, utilizing the same volumetric-deviatoric energy decomposition. Here again, a similar increase in crack width is observed, resulting in a significant portion of the geometry becoming damaged.

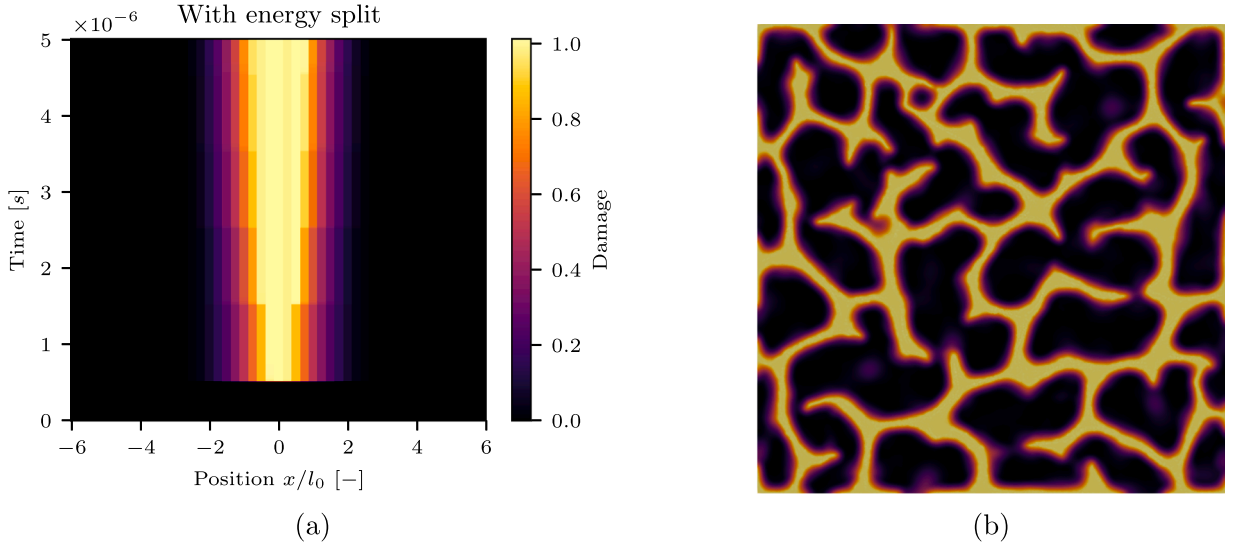

Fig. A.23. (a) c-t diagram of the damage as a function of time and position around the centre of the bar with a volumetric-deviatoric energy split. (b) Fragmentation pattern obtained with a volumetric-deviatoric energy decomposition at $t = 70.7$ ns.

Appendix B. Convergence of wave reflection at a damaged boundary

This appendix presents the convergence analysis of the experiment from Section 4.1 as the regularization length l_0 decreases. Using the base value of $l_0 = 200\,\mu$m from Section 4.1 as a reference, the study evaluates regularization lengths of $l_0/2, l_0/4$ and $l_0/8$.

Fig. B.24 displays the result without mass degradation, following the same format as Fig. 7. To facilitate direct comparison, the horizontal scale for the position remains identical to that in Fig. 7. It is evident that the observed wave reflection converges toward the reference result shown in Fig. 5.

For comparison, Fig. B.25 presents the same convergence test with mass degradation. In this case, the results are consistent across all regularization lengths, indicating that the wave reflection is nearly independent of l_0.

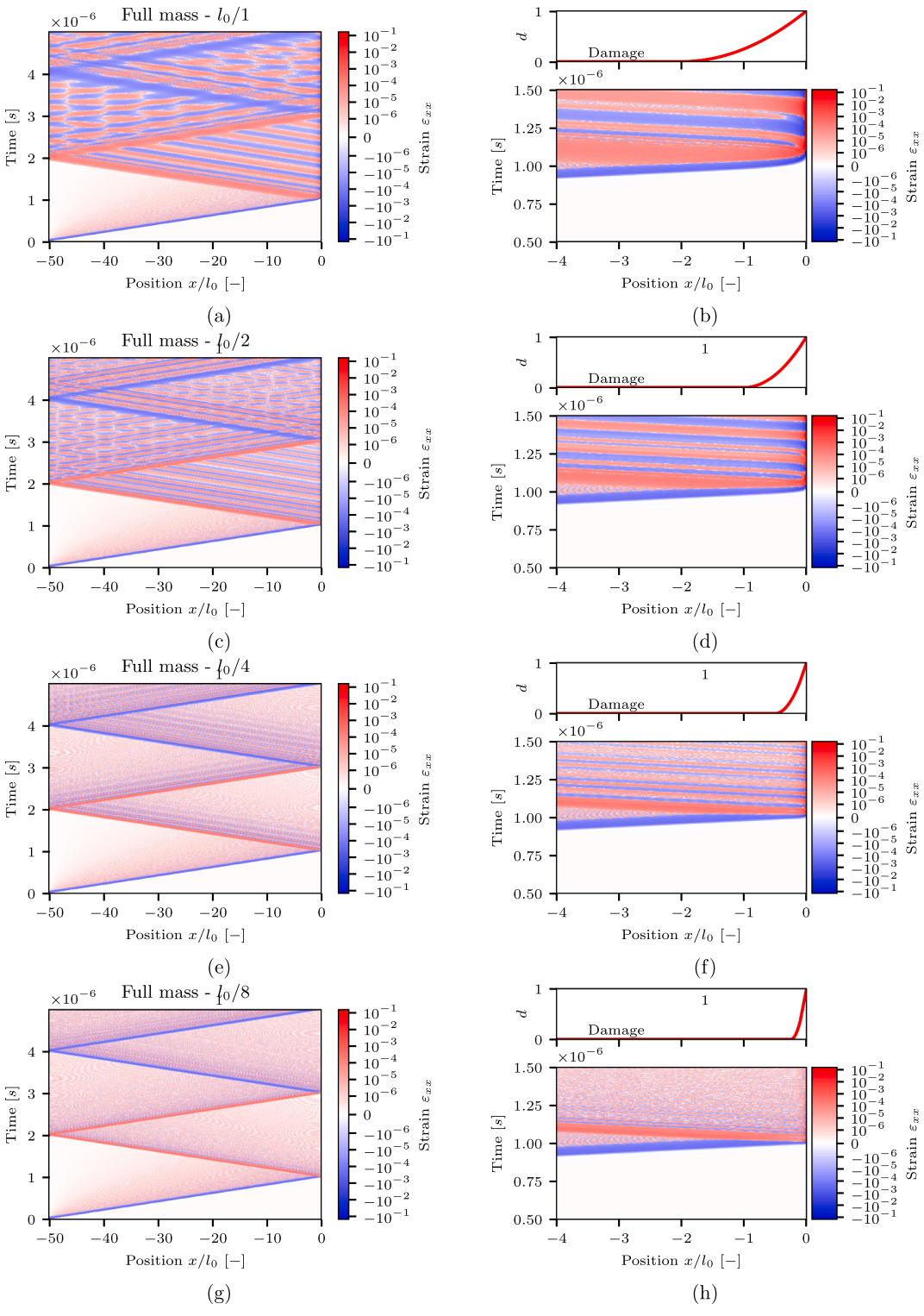

Fig. B.24. Wave reflection at a damaged boundary without mass degradation for decreasing values of l_0.

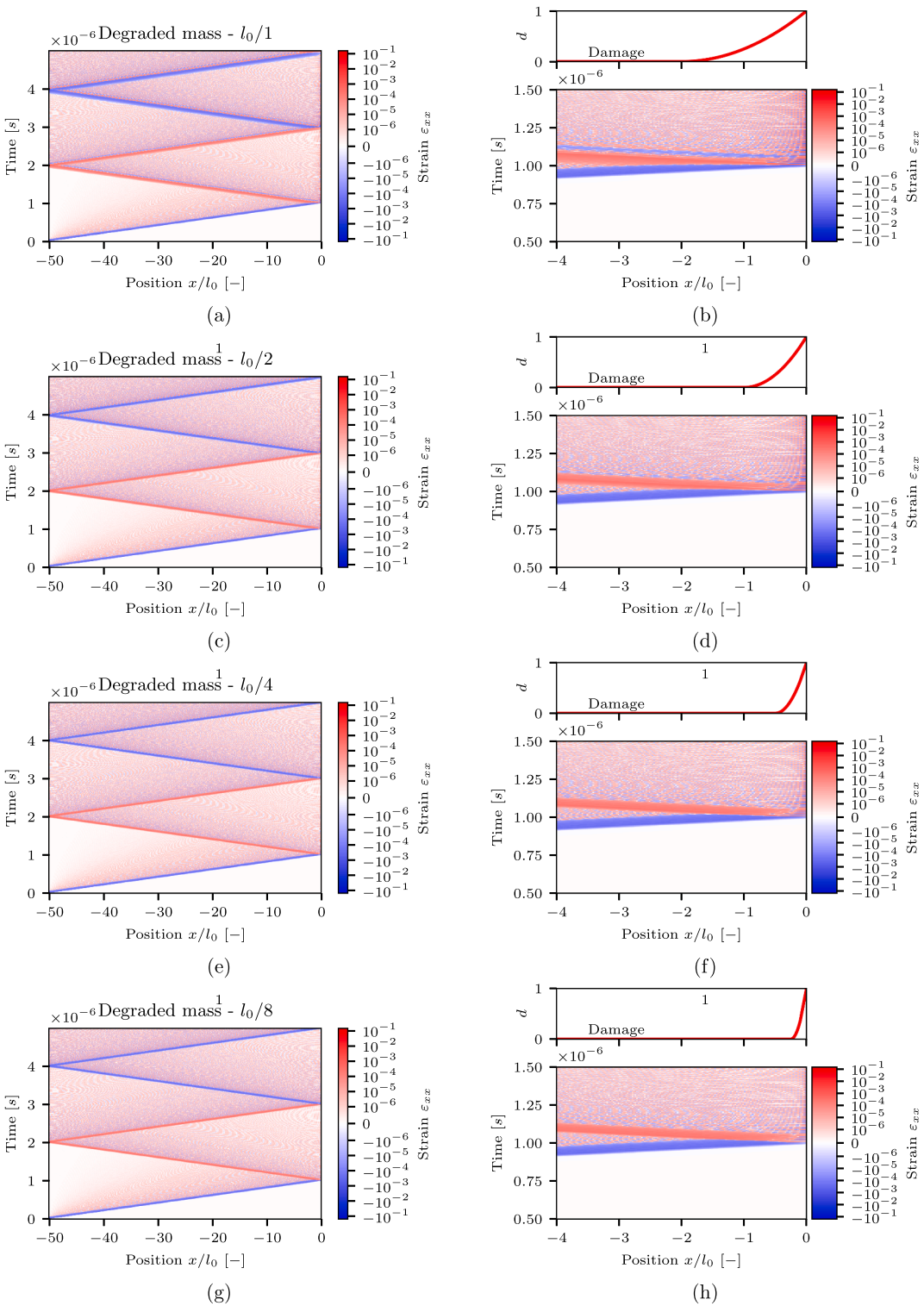

Fig. B.25. Wave reflection at a damaged boundary with mass degradation for decreasing values of l_0.

References

[1] P. Acloque, Deferred processes in the fragmentation of tempered glass, in: Proceedings of the 4Th International Glass Congress, 6, 1956, pp. 279–291.
[2] M. Vocialta, M. Corrado, J.F. Molinari, et al., Numerical analysis of fragmentation in tempered glass with parallel dynamic insertion of cohesive elements, In:Eng. Fracture Mech. 188 (Feb. 1, 2018),pp. 448–469. ISSN:0013-7944. https://doi.org/10.1016/j.engfracmech.2017.09.015
[3] M. Corrado, A.C. Correas, G. Ventura, Phase field fracture model for assessing the load bearing capacity of fractured glass, in: Challenging Glass Conference Proceedings, 9, 2024.
[4] P.H. Krisko, M. Horstman, M.L. Fudge, SOCIT4 Collisional-breakup test data analysis: with shape and materials characterization, Adv. Space Res. 41 (7) (2008) 1138–1146.
[5] F. Morgado, S.A. Peddakotla, C. Garbacz, M.L. Vasile, M. Fossati, Multi-fidelity approach for aerodynamic modelling and simulation of uncontrolled atmospheric destructive entry, in: AIAA SCITECH 2022 Forum, 2022, p. 1323.
[6] N.F. Mott, E.H. Linfoot, A theory of fragmentation. In:AC3348 (1943).
[7] D.E. Grady, D.A. Benson, Fragmentation of metal rings by electromagnetic loading. Exp. Mech. 23 4 (Dec. 1,1983), pp. 393–400. ISSN:1741-2765. https://doi.org/10.1007/BF02330054
[8] L.A. Glenn, A. Chudnovsky, Strain-energy effects on dynamic fragmentation, J. Appl. Phys. 59 (4) (1986) 1379–1380. https://doi.org/10.1063/1.336532.
[9] K.T. Ramesh, J.D. Hogan, J. Kimberley, A. Stickle, A review of mechanisms and models for dynamic failure, strength, and fragmentation, Planet Space Sci. 107 (2015) 10–23.
[10] F. Kun, H.J. Herrmann, A study of fragmentation processes using a discrete element method, Comput. Methods Appl. Mech. Eng. 138 (1–4) (1996) 3–18.
[11] F. Wittel, F. Kun, H.J. Herrmann, B.H. Kröplin, Fragmentation of shells, Phys. Rev. Lett. 93 (3) (2004) 035504.
[12] N. Moës, J. Dolbow, T. Belytschko, A finite element method for crack growth without remeshing, Int. J. Numer. Methods Eng. 46 (1) (1999) 131–150.
[13] T. Belytschko, H. Chen, J. Xu, G. Zi, Dynamic crack propagation based on loss of hyperbolicity and a new discontinuous enrichment, Int. J. Numer. Methods Eng. 58 (12) (2003) 1873–1905.
[14] D.S. Dugdale, Yielding of steel sheets containing slits, J. Mech. Phys. Solids 8 (2) (1960) 100–104.
[15] G.I. Barenblatt, The mathematical theory of equilibrium cracks in brittle fracture, Adv. Appl. Mech. 7 (1962) 55–129.
[16] X.-P. Xu, A. Needleman, Numerical simulations of fast crack growth in brittle solids, J. Mech. Phys. Solids 42 (9) (1994) 1397–1434.
[17] G.T. Camacho, M. Ortiz, Computational modelling of impact damage in brittle materials. Int. J. Solids Struct.. 33 20 (Aug. 1, 1996). pp. 2899–2938. ISSN:0020-7683 https://doi.org/10.1016/0020-7683(95)00255-3
[18] M. Ortiz, A. Pandolfi, Finite-deformation irreversible cohesive elements for three-dimensional crack-propagation analysis, Int. J. Numer. Methods Eng. 44 (9) (1999) 1267–1282.
[19] F. Zhou, J.-F. Molinari, K.T. Ramesh, A cohesive model based fragmentation analysis: effects of strain rate and initial defects distribution, Int. J. Solids Struct. 42 (18) (2005) 5181–5207. https://doi.org/10.1016/j.ijsolstr.2005.02.009
[20] M. Vocialta, N. Richart, J.F. Molinari, et al., 3D Dynamic fragmentation with parallel dynamic insertion of cohesive elements. In:Int. J. Numer. Method. Eng.109 12(2017). _eprint:, 1655–1678.ISSN:1097-0207 https://doi.org/10.1002/nme.5339
[21] G. Pijaudier-Cabot, Z.P. Bažant, Nonlocal damage theory, J. Eng. Mech. 113 (10) (1987) 1512–1533.
[22] M. Jirasek, Nonlocal models for damage and fracture: comparison of approaches, Int. J. Solids Struct. 35 (31–32) (1998) 4133–4145.
[23] F. Bobaru, G. Zhang, Why do cracks branch? a peridynamic investigation of dynamic brittle fracture, Int. J. Fract. 196 (1) (2015) 59–98.
[24] N. Moës, C. Stolz, P.-E. Bernard, N. Chevaugeon, A level set based model for damage growth: the thick level set approach, Int. J. Numer. Methods Eng. 86 (3) (2011) 358–380.
[25] N. Chevaugeon, N. Moës, Lipschitz regularization for fracture: the lip-field approach, Comput. Methods Appl. Mech. Eng. 402 (2022) 115644.
[26] A. Karma, D.A. Kessler, H. Levine, et al., Phase-Field model of mode III dynamic fracture.In:Phys. Rev. Lett. 87 (4) (July 3,2001) 045501. Publisher: American Physical Society, https://doi.org/10.1103/PhysRevLett.87.045501
[27] H. Henry, Study of the branching instability using a phase field model of inplane crack propagation. In:EPL.83 1 (June 2008).p. 16004. ISSN:0295-5075. https://doi.org/10.1209/0295-5075/83/16004
[28] A.A. Griffith, Griffith-The phenomena of rupture and flow in solids, Philos. Trans. R. Soc. Lond. Ser. A, Contain. Paper. Math. Phys. Charcter 221 (1921) 163–198.
[29] G.A. Francfort, J.J. Marigo, Revisiting brittle fracture as an energy minimization problem.In:J. Mech. Phys. Solids. 46 8 (Aug. 1, 1998), pp. 1319–1342. ISSN:0022-5096. https://doi.org/10.1016/S0022-5096(98)00034-9
[30] L. Ambrosio, V.M. Tortorelli, Approximation of functional depending on jumps by elliptic functional via t-convergence. In: Commun. Pure Appl. Math. 43 8 (1990). pp. 999–1036.ISSN:1097-0312. _eprint: https://doi.org/10.1002/cpa.3160430805
[31] B. Bourdin, G.A. Francfort, J.J. Marigo, Numerical experiments in revisited brittle fracture. In:J. Mech. Phys. Solids 48 4 (2000), pp. 797–826. ISSN-0022-5096. https://doi.org/10.1016/S0022-5096(99)00028-9
[32] G. Molnár, A. Doitrand, R. Estevez, A. Gravouil, Toughness or strength? regularization in phase-field fracture explained by the coupled criterion, Theor. Appl. Fract. Mech. 109 (2020) 102736.
[33] M. Ambati, T. Gerasimov, L. De Lorenzis, Phase-field modeling of ductile fracture, Comput. Mech. 55 (5) (2015) 1017–1040.
[34] T. Gerasimov, U. Römer, J. Vondřejc, H.G. Matthies, L. De Lorenzis, et al., Stochastic phase-field modeling of brittle fracture: computing multiple crack patterns and their probabilities. In:Comput. Method. Appl. Mech. Eng. 372 (Dec. 1, 2020), p, 113353.ISSN:0045-7825. https://doi.org/10.1016/j.cma.2020.113353
[35] M.J. Borden, C.V. Verhoosel, M.A. Scott, T.J.R. Hughes, C.M. Landis, et al., A phase-field description of dynamic brittle fracture. In: Comput. Method. Appl. Mech. Eng. 217–220 (Apr. 1, 2012), pp. 77–95. ISSN:0045-7825. https://doi.org/10.1016/j.cma.2012.01.008
[36] T. Li, J.-J. Marigo, D. Guilbaud, S. Potapov, et al., Gradient damage modeling of brittle fracture in an explicit dynamics context. In:Int. J. Numer. Method. Eng. 108 11 (2016). pp. 1381–1405. ISSN:1097-0207. _eprint: https://doi.org/10.1002/nme.5262
[37] A. Geromel Fischer, J.-J. Marigo, Gradient damage models applied to dynamic fragmentation of brittle materials: a. geromel fischer, j.-J. marigo, Int. J. Fract. 220 (2) (2019) 143–165.
[38] G.D. Huynh, R. Abedi, Rate dependency and fragmentation response of phase field models with micro inertia and micro viscosity terms, J. Mech. Phys. Solids 196 (2025) 105971. https://doi.org/10.1016/j.jmps.2024.105971
[39] K. Weinberg, C. Wieners, Dynamic phase-field fracture with a first-order discontinuous galerkin method for elastic waves, Comput. Methods Appl. Mech. Eng. 389 (2022) 114330. https://doi.org/10.1016/j.cma.2021.114330
[40] M.J. Borden, T.J.R. Hughes, C.M. Landis, C.V. Verhoosel, A higher-order phase-field model for brittle fracture: formulation and analysis within the isogeometric analysis framework, Comput. Methods Appl. Mech. Eng. 273 (2014) 100–118.
[41] K. Pham, H. Amor, J.-J. Marigo, C. Maurini, et al., Gradient damage models and their use to approximate brittle fracture. In:Int. J. Damage Mech. 20 4 (May 1, 2011). pp. 618–652.ISSN:1056-7895. Publisher: SAGE Publications Ltd STM, https://doi.org/10.1177/1056789510386852
[42] H. Amor, J.-J. Marigo, C. Maurini, et al., Regularized formulation of the variational brittle fracture with unilateral contact: numerical experiments. In:J. Mech. Phys. Solids 57 8 (Aug. 1, 2009), pp. 1209–1229.ISSN:0022-5096. https://doi.org/10.1016/j.jmps.2009.04.011
[43] C. Miehe, M. Hofacker, F. Welschinger, et al., A phase field model for rate-independent crack propagation: robust algorithmic implementation based on operator splits. In:Comput. Method. Appl. Mech. Eng. 199 45 (Nov. 15, 2010), pp. 2765–2778.ISSN:0045-7825. https://doi.org/10.1016/j.cma.2010.04.011
[44] F. Vicentini, C. Zolesi, P. Carrara, C. Maurini, L. De Lorenzis, On the energy decomposition in variational phase-field models for brittle fracture under multi-axial stress states, Int. J. Fract. (2024). https://doi.org/10.1007/s10704-024-00763-w
[45] N.F. Mott, Fragmentation of shell cases, Proc. R. Soc. Lond. Ser. A. Math. Phys. Sci. 189 (1018) (1947) 300–308.
[46] F. Zhou, J.-F. Molinari, K.T. Ramesh, A cohesive model based fragmentation analysis: effects of strain rate and initial defects distribution, Int. J. Solids Struct. 42 (18–19) (2005) 5181–5207.

[47] C.-H. Chen, E. Bouchbinder, A. Karma, et al., Instability in dynamic fracture and the failure of the classical theory of cracks. In:Nature Phys. 13 12 (Dec. 2017). pp. 1186–1190. ISSN:1745-2481. Number: 12 Publisher: Nature Publishing Group, https://doi.org/10.1038/nphys4237
[48] A. Vasudevan, Y. Lubomirsky, C.-H. Chen, E. Bouchbinder, A. Karma, Oscillatory and tip-splitting instabilities in 2D dynamic fracture: the roles of intrinsic material length and time scales, J. Mech. Phys. Solids 151 (2021) 104372. https://doi.org/10.1016/j.jmps.2021.104372
[49] N. Richart, G. Anciaux, E. Gallyamov, L. Frérot, D. Kammer, M. Pundir, M. Vocialta, A.C. Ramos, M. Corrado, P. Müller, F. Barras, S. Zhang, R. Ferry, S. Durussel, J.-F. Molinari, Akantu: an HPC finite-element library for contact and dynamic fracture simulations, J. Open Source Softw. 9 (94) (2024) 5253. https://doi.org/10.21105/joss.05253
[50] S. Balay, S. Abhyankar, M.F. Adams, S. Benson, J. Brown, P. Brune, K. Buschelman, E. Constantinescu, L. Dalcin, A. Dener, V. Eijkhout, J. Faibussowitsch, W.D. Gropp, V. Hapla, T. Isaac, P. Jolivet, D. Karpeev, D. Kaushik, M.G. Knepley, F. Kong, S. Kruger, D.A. May, L.C. McInnes, R.T. Mills, L. Mitchell, T. Munson, J.E. Roman, K. Rupp, P. Sanan, J. Sarich, B.F. Smith, H. Suh, S. Zampini, H. Zhang, H. Zhang, J. Zhang, PETSc/TAO Users Manual, Technical Report ANL-21/39 - Revision 3.23, Argonne National Laboratory, 2025. https://doi.org/10.2172/2476320
[51] S. Balay, W.D. Gropp, L.C. McInnes, B.F. Smith, Efficient management of parallelism in object oriented numerical software libraries, in: E. Arge, A.M. Bruaset, H.P. Langtangen (Eds.), Modern Software Tools in Scientific Computing, Birkhäuser Press, 1997, pp. 163–202.
[52] T. Munson, J. Sarich, S. Wild, S. Benson, L.C. McInnes, Toolkit for Advanced Optimization (TAO) Users Manual, Technical Report ANL/MCS-TM-322 - Revision 3.5, Argonne National Laboratory, 2014. https://www.mcs.anl.gov/research/projects/tao/.
[53] J.J. Moré, G. Toraldo, On the solution of large quadratic programming problems with bound constraints, SIAM J. Optim. 1 (1) (1991) 93–113. https://doi.org/10.1137/0801008
[54] N. Richart, J.F. Molinari, Implementation of a parallel finite-element library: test case on a non-local continuum damage model. In:Finite Element. Anal. Des. 100 (Aug. 1, 2015). pp. 41–46.ISSN:0168-874X. https://doi.org/10.1016/j.finel.2015.02.003
[55] J. Bleyer, C. Roux-Langlois, J.-F. Molinari, et al., Dynamic crack propagation with a variational phase-field model: limiting speed, crack branching and velocity-toughening mechanisms. In:Int. J. Fract. 204 1 (Mar. 1, 2017), pp. 79–100. ISSN:1573-2673. https://doi.org/10.1007/s10704-016-0163-1
[56] F. Zhou, Study on the macroscopic behavior and the microscopic process of dynamic crack propagation, Ph.D. thesis, The University of Tokyo, Tokyo, 1996. https://doi.org/10.11501/3127347
[57] F. Loiseau, V. Lazarus, How to introduce an initial crack in phase field simulations to accurately predict the linear elastic fracture propagation threshold?, J. Theor. Comput. Appl. Mech. (2025). https://doi.org/10.46298/jtcam.15198
[58] E. Sharon, J. Fineberg, Confirming the continuum theory of dynamic brittle fracture for fast cracks, Nature 397 (6717) (1999) 333–335.
[59] A. Livne, O. Ben-David, J. Fineberg, Oscillations in rapid fracture, Phys. Rev. Lett. 98 (2007) 124301. https://doi.org/10.1103/PhysRevLett.98.124301
[60] H. Henry, H. Levine, Dynamic instabilities of fracture under biaxial strain using a phase field model. In:Phys. Rev. Lett. 93 10 (Sep. 2, 2004). Publisher: American Physical Society,p. 105504. https://doi.org/10.1103/PhysRevLett.93.105504(Visited on 06/19/2013).
[61] A. Karma, A.E. Lobkovsky, Unsteady Crack Motion and Branching in a Phase-Field Model of Brittle Fracture. In:Phys. Rev. Lett. 92 24 (June 18, 2004). p.245510. Publisher: American Physical Society, https://doi.org/10.1103/PhysRevLett.92.245510(Visited on 06/19/2013).
[62] Y. Leng, L. Svolos, I. Boureima, G. Manzini, J.N. Plohr, H.M. Mourad, Arbitrary order virtual element methods for high-Order phase-Field modeling of dynamic fracture, Int. J. Numer. Methods Eng. 126 (1) (2025) e7605.
[63] B. Bourdin, J.-J. Marigo, C. Maurini, C. Zolesi, A variational approach to fracture incorporating any convex strength criterion, arXiv:2506.22558 (2025).
[64] F. Vicentini, J. Heinzmann, P. Carrara, L. De Lorenzis, Variational phase-field modeling of cohesive fracture with flexibly tunable strength surface, J. Mech. Phys. Solids 207 (2026) 106424. https://doi.org/10.1016/j.jmps.2025.106424